ACSNANO

www.acsnano.org

ARTICLE

Delivery of mRNA Encoding Interleukin-12 and a Stimulator of Interferon Genes Agonist Potentiates Antitumor Efficacy through Reversing T Cell Exhaustion

Bin Wang,[⊥] Maoping Tang,[⊥] Qijing Chen, William Ho, Yilong Teng, Xiaojian Xiong, Zhitong Jia, Xiuling Li,* Xiaoyang Xu,* and Xue-Qing Zhang*

Cite This: *ACS Nano* 2024, 18, 15499−15516

Read Online

ACCESS | Metrics & More | Article Recommendations | Supporting Information

ABSTRACT: **T cell exhaustion has emerged as a major hurdle that impedes the clinical translation of stimulator of interferon genes (STING) agonists. It is crucial to explore innovative strategies to rejuvenate exhausted T cells and potentiate the antitumor efficacy. Here, we propose an approach utilizing MSA-2 as a STING agonist, along with nanoparticle-mediated delivery of mRNA encoding interleukin-12 (IL-12) to restore the function of T cells. We developed a lipid nanoparticle (DMT7-*IL12* LNP) that encapsulated *IL12* mRNA. Our findings convincingly demonstrated that the combination of MSA-2 and DMT7-*IL12* LNP can effectively reverse the exhausted T cell phenotype, as evidenced by the enhanced secretion of cytokines, such as tumor necrosis factor alpha, interferon gamma, and Granzyme B, coupled with reduced levels of inhibitory molecules such as T cell immunoglobulin and mucin domain-3 and programmed cell death protein-1 on CD8+ T cells. Furthermore, this approach led to improved survival and tumor regression without causing any systemic toxicity in melanoma and lung metastasis models. These findings suggest that mRNA encoding IL-12 in conjunction with STING agonists has the potential to confer superior clinical outcomes, representing a promising advancement in cancer immunotherapy.**

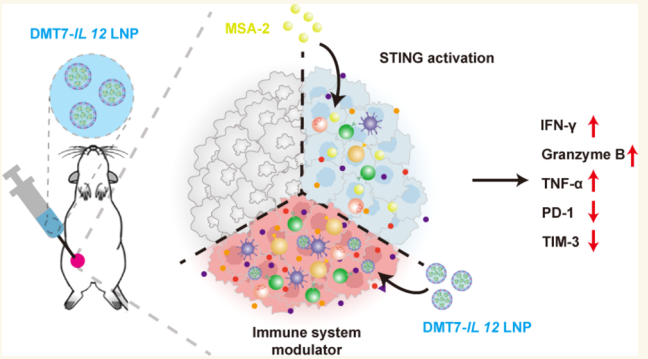

KEYWORDS: *T cell exhaustion, lipid nanoparticles, mRNA therapeutics, STING agonist, cancer immunotherapy*

INTRODUCTION

The pathway involving the stimulator of interferon genes (STING) in dendritic cells (DCs) resident within tumors, once activated, ultimately leads to the generation and release of proinflammatory cytokines and type I interferons. This subsequently amplifies T cell priming and enhances the migration of natural killer (NK) cells and DCs into the tumor microenvironment (TME).[1,2] In recent years, immune-oncology research has primarily concentrated on manipulating the STING pathway to promote agonistic STING responses within the TME. This approach has demonstrated considerable promise in numerous preclinical models for treating solid tumors and hematological malignancies. However, STING agonists, while effective at killing tumor cells in the early stages of tumor progression, elicit only a moderate to poor antitumor immune response in patients with advanced-stage solid tumors. This limitation is primarily due to T cell exhaustion, which poses a significant obstacle to the clinical application of STING agonists in cancer therapy.[3] T cell exhaustion, characterized by a progressive decline in effector functions, persistent expression of inhibitory receptors (such as T cell immunoglobulin and mucin domain-3 (TIM-3) and programmed cell death protein-1 (PD-1)), and diminished cytokine levels (including tumor necrosis factor alpha (TNF-α), Granzyme B, and interferon gamma (IFN-γ)), has been recognized as a significant impediment in achieving durable T cell-dependent tumor immunity.[4] Therefore, there is an unmet

Received: January 2, 2024
Revised: May 19, 2024
Accepted: May 28, 2024
Published: June 4, 2024

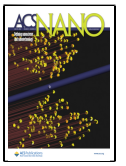

https://doi.org/10.1021/acsnano.4c00063
ACS Nano 2024, 18, 15499−15516

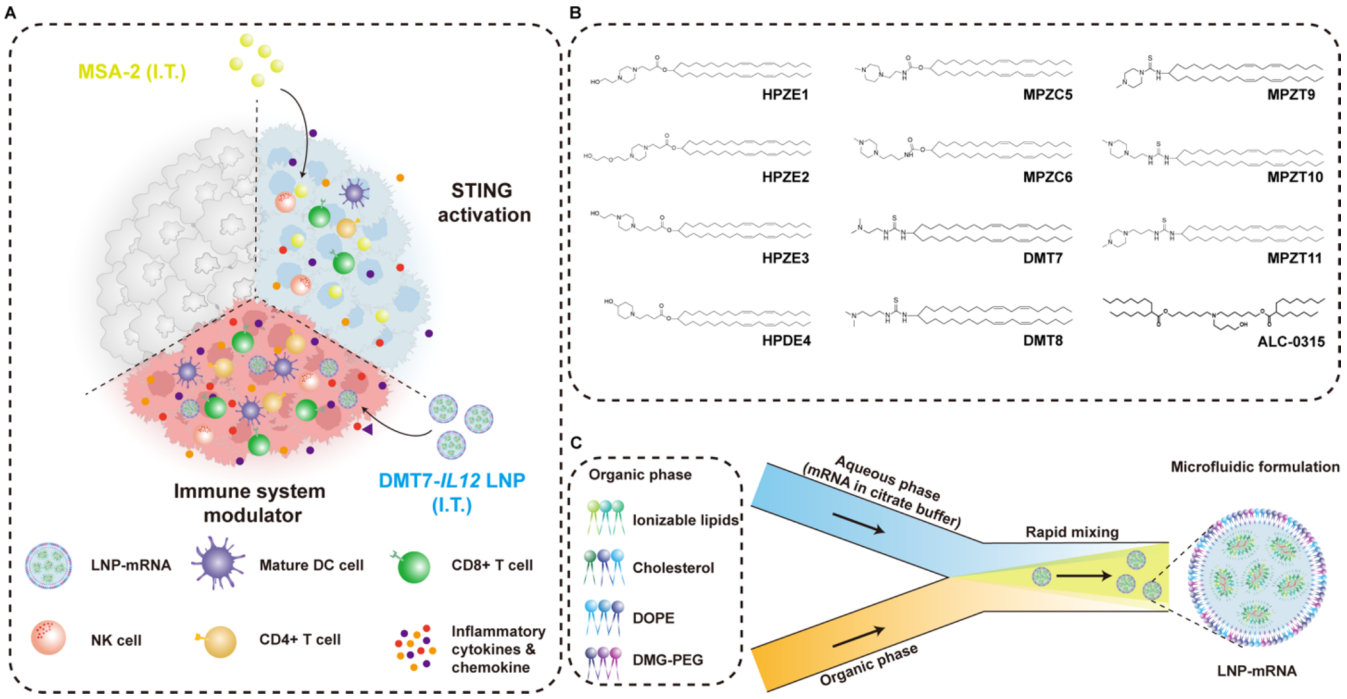

Figure 1. Combinative therapies for enhanced cancer immunotherapy. (A) Illustration of enhanced cancer immunotherapy achieved by utilizing lipid nanoparticles to deliver mRNA encoding cytokines in conjunction with STING agonist-based treatment. (B) The chemical structures of the ionizable lipids and ALC-0315 (C) Preparation of LNP-mRNA using a microfluidic method.

demand to circumvent T cell exhaustion for enhanced antitumor efficiency of immunotherapies, including the use of STING agonists.

We hypothesize that the utilization of an immune system modulator like IL-12, which can stimulate responses against foreign pathogens and reshape the tumor immune microenvironments (TIME), holds promise in mitigating T cell exhaustion, thereby augmenting the antitumor immune response. In this context, we introduce a nanoparticle mRNA therapeutic strategy aimed at restoring the complete effector functionality of T cells that undergo exhaustion following priming by STING agonist-based therapy. Specifically, the sequential administration of MSA-2, a potent second-generation STING agonist with strong binding affinity for both mouse and human STING,[5] followed by lipid nanoparticle (LNP)-encapsulated mRNA encoding IL-12 (*IL12* mRNA) to the TME, constitutes a two-step stimulation strategy. MSA-2 initiates an innate immune response in the first step, facilitating the influx of nonexhausted T cells into tumors.[6−8] Subsequently, the IL-12-driven adaptive immune response activates the cytotoxic functions of CD8+ T cells and further shields them from exhaustion, sustaining the antitumor activity of T cells. This groundbreaking strategy offers a potentially universal solution for reversing T cell exhaustion, effectively reprogramming the TIME into a highly inflamed phenotype, exhibits a synergistic effect with STING agonists, and presents a versatile treatment option for a wide variety of tumor types.

IL-12, a cytokine initially identified as a growth factor for T cells, has been shown to not only stimulate the proliferation and effector functions of NK and CD8+ T cells but also facilitate the T helper 1 (Th1) cell differentiation and IFN-γ production.[9−12] While possessing promising antitumor immune properties, the clinical translation of recombinant IL-12 has been hindered by its short half-life in the bloodstream (approximately 30 min) and the potential toxicity associated with high-dose systemic administration.[13,14] Therefore, it is crucial to devise strategies that enable sustained local expression of bioactive IL-12 to maintain prolonged antitumor effects within the TME.[15,16] With the rapid advancement of mRNA technology, mRNA has surfaced as a promising therapeutic option for a multitude of diseases.[17,18] To address the challenges associated with the clinical use of IL-12, it is imperative to develop nanocarriers facilitating the delivery of mRNA therapeutics, such as *IL12* mRNA, to the TME. This approach aims to alleviate T cell exhaustion and induce a robust adaptive immune response for improved cancer immunotherapy.

To achieve this goal, we have formulated and synthesized a collection of innovative ionizable lipids. Among them, DMT7 emerged as a highly effective ionizable lipid for the formulation of mRNA-loaded LNPs. The combination immunotherapy strategy, which involves sequential intratumoral delivery of MSA-2 followed by DMT7-*IL12* LNPs, significantly boosts the number of CD8+ T cells that produce cytokines (Granzyme B, TNF-α, and IFN-γ) within the TME of B16F10 tumor-bearing mice. This approach also diminishes the expression of inhibitory molecules such as TIM-3 and PD-1 on CD8+ T cells, indicating a reversal of T cell exhaustion in the immunosuppressive TME (Figure 1A). The overall antitumor activity of this combination immunotherapy strategy was further evaluated in both B16F10 and 4T1 tumor models. The findings clearly demonstrate a significant enhancement in antitumor responses in untreated contralateral tumors and lung metastases compared to treatment with DMT7-*IL12* LNPs or MSA-2 alone. Notably, the sequential intratumoral delivery of MSA-2 and DMT7-*IL12* LNPs synergizes with anti-PD-1 (αPD-1) therapy to enhance antitumor immune responses. These findings highlight the translational potential of this combinatorial approach for antitumoral immunotherapy. It is

https://doi.org/10.1021/acsnano.4c00063
ACS Nano 2024, 18, 15499−15516

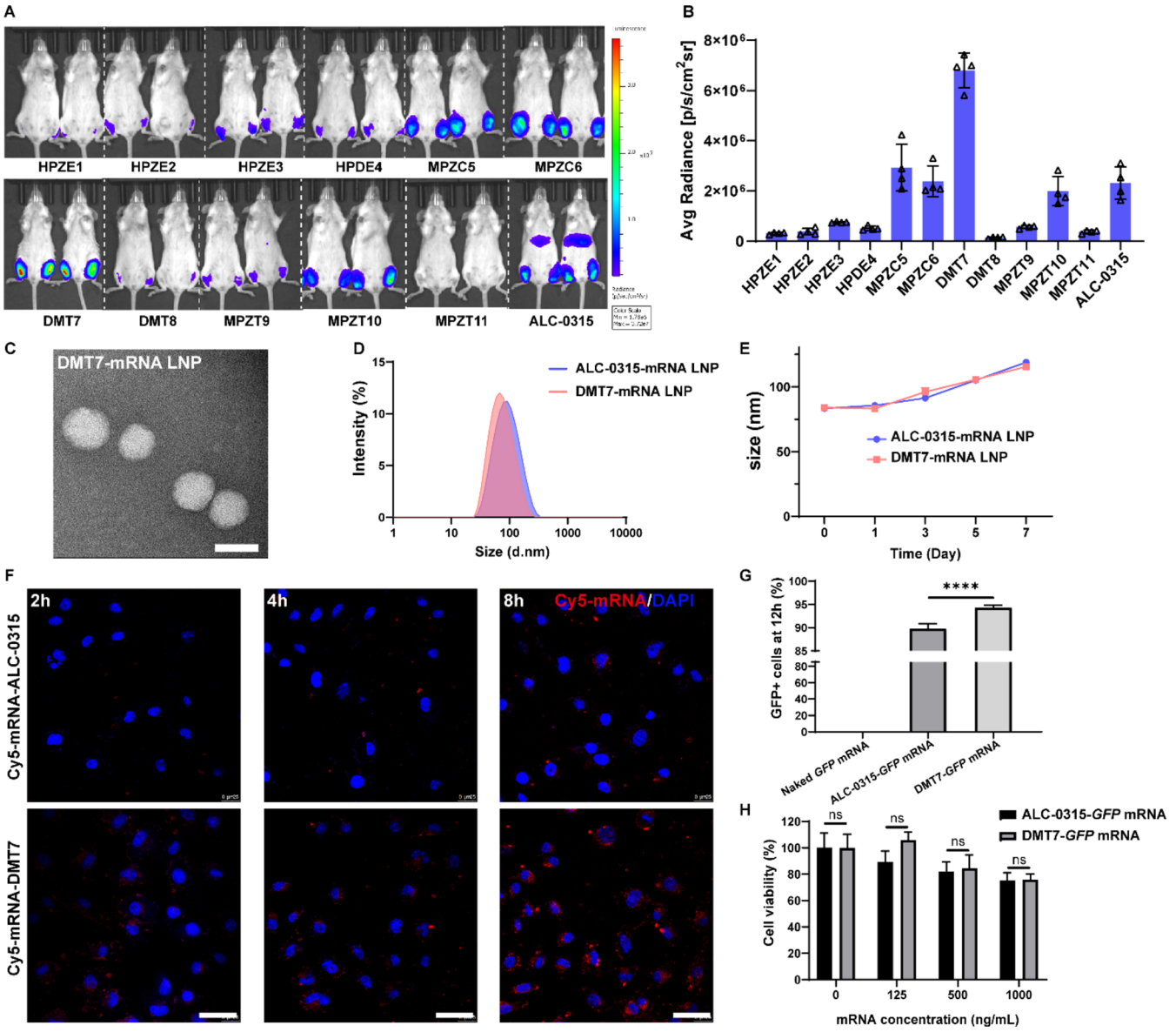

Figure 2. (A) Representative bioluminescence images of mice were obtained following intramuscular injection of *FLuc* mRNA-loaded LNPs. (B) Semiquantification of luminescence intensity in (A) (n = 4). (C) Representative TEM images of DMT7-mRNA. Scale bar, 50 nm. (D) The size distribution of ALC-0315-mRNA and DMT7-mRNA detected by DLS. (E) The size change of ALC-0315-mRNA and DMT7-mRNA in PBS during evaluation over 7 days (n = 4). (F) Cellular uptake of Cy5-labeled mRNA encapsulated in ALC-0315/DMT7 LNPs (red) was evaluated at various time points. (G) Flow cytometry analysis of GFP expression in B16F10 cells (n = 4), significant differences were assessed using a one-way ANOVA with Tukey test, ****p < 0.0001, data are presented as mean ± SD. (H) Cytotoxicity of DMT7 and ALC-0315 LNPs was evaluated in B16F10 cells (n = 6), and no significant difference was observed in the cytotoxicity between DMT7 LNPs and ALC-0315 LNPs.

worth noting that this mRNA-LNP approach for reversing T cell exhaustion could potentially be applied to other cancer immunotherapies, including CAR-T (Chimeric Antigen Receptor Engineered T cell) or TCR (T cell receptor) therapies, to enhance therapeutic efficacy.

RESULTS

Design, Synthesis, and Screening of Ionizable Lipids for mRNA Delivery. We have rationally designed a series of ionizable lipids consisting of piperazine and piperidine derivatives as ionizable headgroups, which are chemically bound to hydrophobic linoleic acid chains through different biodegradable linkers containing a thiourea or carbamate bond. As shown in Figure 1B, we successfully synthesized 11 ionizable lipids following the representative synthetic routes shown in Figures S1−S4, and mass spectroscopy (MS) and nuclear magnetic resonance (NMR) were utilized to characterize their chemical structures (Figures S5−S15). We also synthesized mRNAs encoding Firefly luciferase (*FLuc* mRNA), green fluorescence protein mRNA (*GFP* mRNA), and interleukin-12 mRNA (*IL12* mRNA), respectively, using an in vitro transcription method as described previously.[19] To construct LNPs, the synthesized ionizable lipids were combined with mRNA, PEG-lipid conjugates, 1,2-dioleoyl-*sn*-glycero-3-phosphoethanolamine (DOPE) phospholipid, and cholesterol using a microfluidic method (Figure 1C). Dynamic light scattering (DLS) results indicate that *FLuc* mRNA-LNPs

https://doi.org/10.1021/acsnano.4c00063
ACS Nano 2024, 18, 15499−15516

have a neutral ζ-potential (Figure S16), and their sizes range from 55 to 90 nm, with a polydispersity index (PDI) value of less than 0.2 (Figure S17). The pK_a values of different LNPs were all within the range of 5−9 (Table S1). The encapsulation efficiency of most obtained LNPs was over 80%, and DMT7 LNP showed the highest mRNA encapsulation efficiency (95.3%) (Table S2). We further studied the in vivo transfection efficiency of different LNPs through intramuscular injection of LNPs formulated with *FLuc* mRNA and found that DMT7 LNP displayed the highest mRNA delivery efficiency (Figure 2A). The transfection efficiency of DMT7 LNP is 2.8-fold higher than that of ALC-0315 LNP, a commercial mRNA delivery system that has been widely used in the production of COVID-19 mRNA vaccines[20−22] (Figure 2B). Overall, these results suggest that after screening for in vivo transfection efficiency, a potent LNP (DMT7 LNP) with high mRNA delivery efficiency was identified for further investigation.

In Vitro Assessment of DMT7 LNP-Mediated mRNA Transfection and Cytotoxicity. As shown in Figure 2C, the DMT7-*IL12* mRNA LNP exhibited a uniform and spherical structure under transmission electron microscopy (TEM), and the hydrodynamic diameter of DMT7-*IL12* mRNA LNP was similar to ALC-0315-*IL12* mRNA LNP (Figure 2D). To assess the ability of the DMT7 LNP to protect mRNA from degradation by nucleases that are abundant in the tumor microenvironment (TME), we tested the stability of mRNA encapsulated within the DMT7 LNP under different conditions. As illustrated in Figure S18, in comparison to the PBS treatment group, the levels of IL-12 p70 expression in tumor tissues exhibit a notable increase at 6 h post intratumoral administration of DMT7-*IL12* mRNA, which gradually declines over time. Nevertheless, there persists a substantial expression level of nearly 30% even after 72 h. The mRNA encapsulated within the DMT7 LNP demonstrated good stability when incubated with 10% fetal bovine serum (FBS) or 10 ng/mL RNase for up to 24 h when in its free form, the mRNA rapidly degraded within 5 min, as shown in Figures S19 and S20. Notably, there was a gradual increase in particle size over 7 days when the DMT7-*IL12* LNP was incubated in PBS at 37 °C to mimic a physiological environment (Figure 2E). The transfection and expression efficacy of DMT7-*IL12* LNP in B16F10 and 4T1 cell lines were analyzed by ELISA. The results reveal a significantly elevated expression of IL-12 at 24 h, which subsequently decreases over time; nonetheless, there remains a nearly 40% expression level even after 7 days (Figure S21). Additionally, we monitored turbidity to assess the stability of the mRNA-DMT7 LNP in serum, and as shown in Figure S22, no observable aggregation was found, indicating its stability at room temperature (RT) or 37 °C in the presence of serum. Collectively, these findings suggest that the developed DMT7 LNP possesses a stable nanostructure capable of effectively shielding the encapsulated mRNA from degradation over a specific duration.

We subsequently conducted confocal laser scanning microscopy to explore the intracellular uptake and trafficking processes of the DMT7 LNP in B16F10 cells, using ALC-0315 LNP as a positive control. The Cy5-labeled *FLuc* mRNA was encapsulated into both the ALC-0315 and DMT7 LNPs (denoted as Cy5-*FLuc* mRNA-ALC-0315 or Cy5-*FLuc* mRNA-DMT7). B16F10 cells were incubated with these Cy5-*FLuc* mRNA-LNPs for 2, 4, or 8 h. Figures 2F and S23 demonstrate that Cy5-*FLuc* mRNA-LNPs are effectively internalized into tumor cells and undergo lysosomal escape in a time-dependent manner. To elucidate the endocytic routes implicated in the cellular uptake of the DMT7 LNP, we transfected B16F10 cells with DMT7 LNP encapsulating *GFP* mRNA after treating them with various endocytic inhibitors. The inhibitors utilized in our study included 5-(*N*-methyl-*N*-isopropyl) amiloride (EIPA), filipin, and chlorpromazine hydrochlorides (CPZ), responsible for macropinocytosis, caveolae-mediated endocytosis, and clathrin-mediated endocytosis, respectively. Upon exposure to EIPA, GFP expression was notably inhibited by 35%, while CPZ treatment resulted in a more substantial reduction of 56%, while Filipin treatment caused moderate differences in GFP expression (Figure S24). These results suggest that the DMT7 LNP is likely internalized mainly through macropinocytosis and clathrin-mediated endocytic pathways, consistent with previous studies.[23,24] Flow cytometry analysis revealed that *GFP* mRNA-DMT7 LNP increased the average percentage of GFP$^+$ cells by 1.08-fold compared with the *GFP* mRNA-ALC-0315 LNP treatment group (Figures 2G and S25), indicating a superior in vitro transfection efficiency of the DMT7 LNPs. The cytotoxicity of the *GFP* mRNA-DMT7 LNP was determined in B16F10 cells by measuring cell viability after treatment with varying doses of LNPs for 48 h. The data revealed comparable cell viability, even at mRNA concentrations reaching as high as 1000 ng/mL, thereby demonstrating the excellent biocompatibility of the DMT7 LNPs (Figure 2H). We then measured the expression levels of secreted interleukin (IL)-12 p70 via ELISA. The secretion of IL-12 p70 peaked at 12 h after treatment with DMT7-*IL12* LNP (Figure S26). These findings strongly suggest that DMT7 LNP, due to its efficient mRNA delivery and excellent biocompatibility, holds significant potential for mRNA-based therapeutic applications.

Reduced T Cell Exhaustion by DMT7-*IL12* LNP + MSA-2 in TME. Tumor-reactive CD8+ T cells that infiltrate tumors often display a consistent phenotype of exhaustion due to persistent antigen exposure across multiple tumor models.[25−27] In situ vaccination strategies, such as the use of STING agonists, have demonstrated considerable promise in systemically augmenting the population of tumor-reactive T cells.[28] In this work, we first assessed the antitumor effect of MSA-2, a known STING agonist that promotes innate immunity,[2,6,7] in the context of B16F10 murine melanoma—a highly aggressive and immunologically limited tumor model.[29] Notably, while MSA-2 treatment alone did exhibit an antitumor effect in treated tumors 18−20 days postinoculation, it failed to achieve sustained tumor inhibition in both treated and untreated tumors (Figure S27). This limited efficacy is likely attributed to the exhausted phenotype of T cells resulting from STING signaling.[3] To sustain a robust antitumor immune response, modulating the TIME in conjunction with reversing T cell exhaustion through the local delivery of IL-12 via DMT7-*IL12* LNPs may significantly impact immunotherapy outcomes. Once activated, cytotoxic T lymphocytes can execute their effector functions through devious mechanisms. Among these are the secretion of cytolytic molecules, such as granzymes, and the generation of inflammatory cytokines, including TNF-α and IFN-γ.[30,31] To specifically investigate the efficacy of DMT7-*IL12* LNP + MSA-2 in regulating the functional recovery of effector T cells, we administered MSA-2 into the tumor site 24 h prior to the intratumoral injection of DMT7-*IL12* LNP in a B16F10 tumor model (Figure 3). Our findings

https://doi.org/10.1021/acsnano.4c00063
ACS Nano 2024, 18, 15499−15516

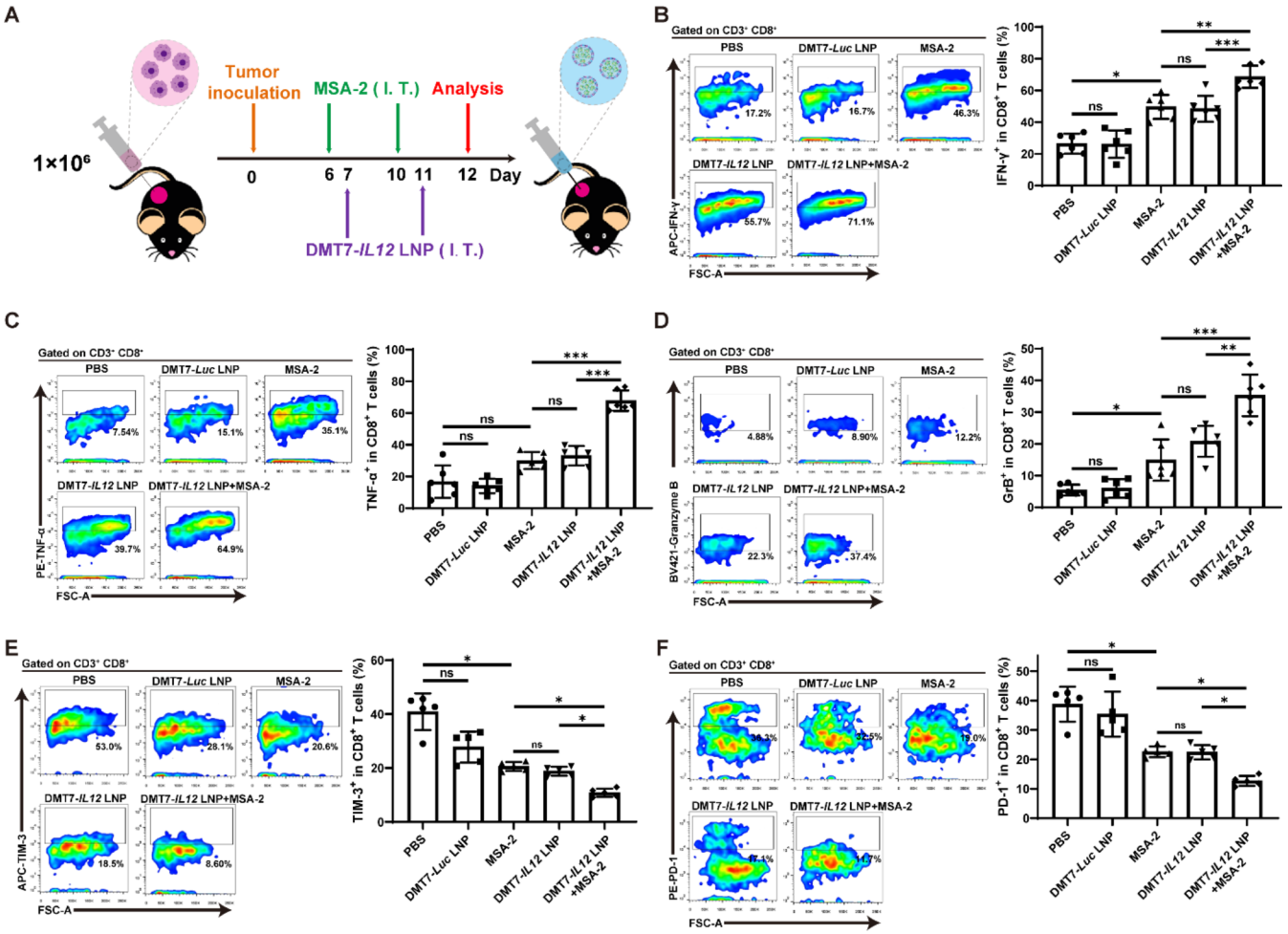

Figure 3. In vivo antitumor immune responses by DMT7-*IL12* LNP with MSA-2 in a B16F10 melanoma model. (A) This diagram illustrates the schedule for immune cell analysis within TME in the B16F10 mouse model. (B–D) Representative flow cytometry dot plots and percentage of IFN-γ+ (B), TNF-α+ (C), and Granzyme B+ (D) cells in CD8+ T cells (CD3 + CD8+), (n = 6), $p > 0.05$ (ns, not significant), $^{**}p < 0.01$ and $^{***}p < 0.001$. (E, F) Representative flow cytometry dot plots and percentage of TIM-3+ (E) and PD-1+ (F) cells in CD8+ T cells (CD3 + CD8+), (n = 5), $^{*}p < 0.05$. All data are presented as mean ± standard deviation (SD) and were analyzed via one-way ANOVA with Tukey's test.

demonstrated that MSA-2 treatment alone resulted in a mere 1.5-fold elevation in the frequency of tumor-infiltrating CD8+ T cells producing cytokines (TNF-α, Granzyme B, and IFN-γ) in comparison to PBS or DMT7-*Luc* LNP treatment. However, a noteworthy observation was made in tumor-bearing mice subjected to DMT7-*IL12* LNP combined with MSA-2 treatment. In these mice, we observed a significant 2.28- to 4.9-fold increase in the frequency of tumor-infiltrating CD8+ T cells secreting cytokines (TNF-α, Granzyme B, and IFN-γ) compared to the groups receiving PBS or DMT7-FLuc LNP treatment (Figure 3B–D). This significant elevation highlights a substantial restoration of T cell function within the TME, emphasizing the heightened antitumor T cell responses triggered by the combined DMT7-*IL12* LNP + MSA-2 treatment.

In the context of continuous exposure to tumor antigens, T cells often enter a state of exhaustion within tumor sites, characterized by increased levels of inhibitory checkpoint receptors such as TIM-3 and PD-1.[32] Therefore, we further explored whether DMT7-*IL12* LNP + MSA-2 could effectively reverse the exhausted phenotype of CD8+ T cells within the TME. As shown in Figure 3E,F, the administration of MSA-2 alone led to a moderate decrease in the level of inhibitory molecules, including TIM-3 and PD-1, on CD8+ T cells within the TME. Although DMT7-*Luc* LNP slightly reduced the expression of TIM-3, probably due to the elevated levels of IL-6 and other proinflammatory cytokines induced by lipid nanoparticles,[33−35] there was no significant difference observed between the PBS and DMT7-*Luc* LNP treatment groups. Notably, in the DMT7-*IL12* LNP + MSA-2-treated group, we observed a significant reduction of 66.6% and 83.3% in the expression of TIM-3 and PD-1 on CD8+ T cells, respectively. This reduction indicates a significant reversal of the exhausted phenotype in CD8+ T cells within the hostile TME. Collectively, these findings presented here clearly demonstrate that the combination of localized MSA-2 administration and the production of bioactive IL-12 through DMT7-*IL12* LNP effectively reverses the exhausted phenotype of CD8+ T cells, redirecting them toward an effector phenotype within the TME. Modulating the TME into a highly inflamed state significantly enhances antitumor T cell responses.

Improved Antitumor Effect of DMT7-*IL12* LNP with MSA-2 in the B16F10 Tumor Model. Building on the improved T cell responses in the TME after DMT7-*IL12* LNP

https://doi.org/10.1021/acsnano.4c00063
ACS Nano 2024, 18, 15499−15516

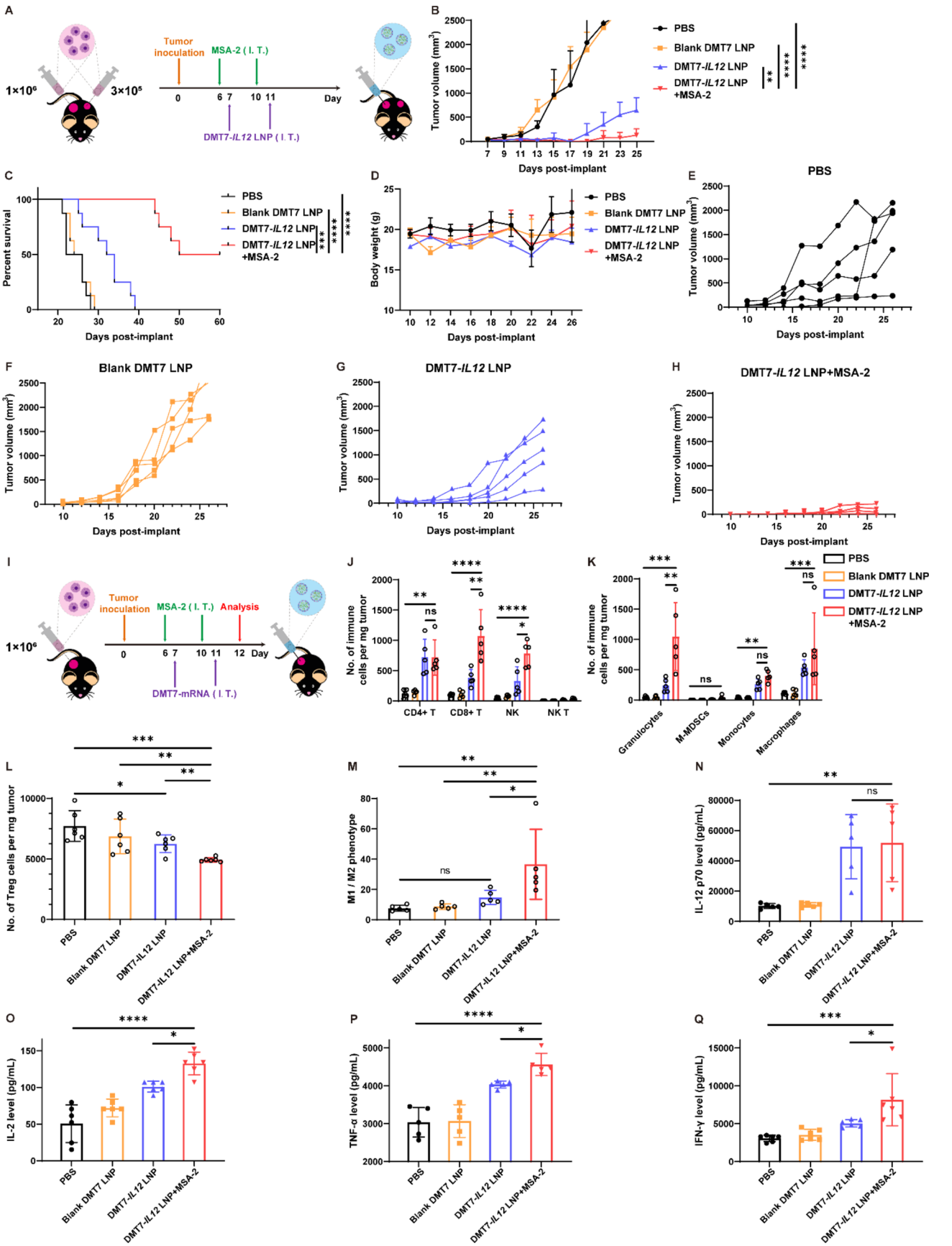

Figure 4. In vivo evaluation of antitumor activity of DMT7-*IL12* LNP with MSA-2 in a B16F10 melanoma model. (A) Schematic illustration of the treatment regimen for the antitumor study. (B, C) Average tumor growth at the treated side (B) and Kaplan−Meier survival curves (C) of B16F10 melanoma−bearing mice with different treatments (n = 8). (D) Body weight changes following intratumoral administration of the indicated treatment groups. (E−H) Tumor volumes of individual mice at the untreated side. (I) Schematic illustration of the

https://doi.org/10.1021/acsnano.4c00063
ACS Nano 2024, 18, 15499−15516

Figure 4. continued

treatment regimen for flow cytometry analysis. (J, K) Flow cytometry analysis of the immune composition of leukocytes in tumors 24 h after intratumoral injection of the indicated treatment groups. (L and M) The ratio of CD4 + CD25 + Foxp3 + Treg cell filtration and M2 polarization of macrophages toward the M1 phenotype in tumors 24 h after intratumoral injection of the indicated treatment groups. (N−Q) ELISA analysis of IL-12 (N), IL-2 (O), TNF-α (P), and IFN-γ (Q) expression in 200 mg of B16F10 tumor tissues (n = 6). Significant differences were evaluated using a one-way ANOVA with Tukey's test (B, J, K, L, M, and N−Q). For the survival curve, statistical significance was determined using the log-rank test (C). Data in (B, D, J, K, L, M, and N−Q) are presented as mean ± SD. The level of significance is indicated as follows: $p > 0.05$ (ns, not significant), *$p < 0.05$, **$p < 0.01$, ***$p < 0.001$, and ****$p < 0.0001$.

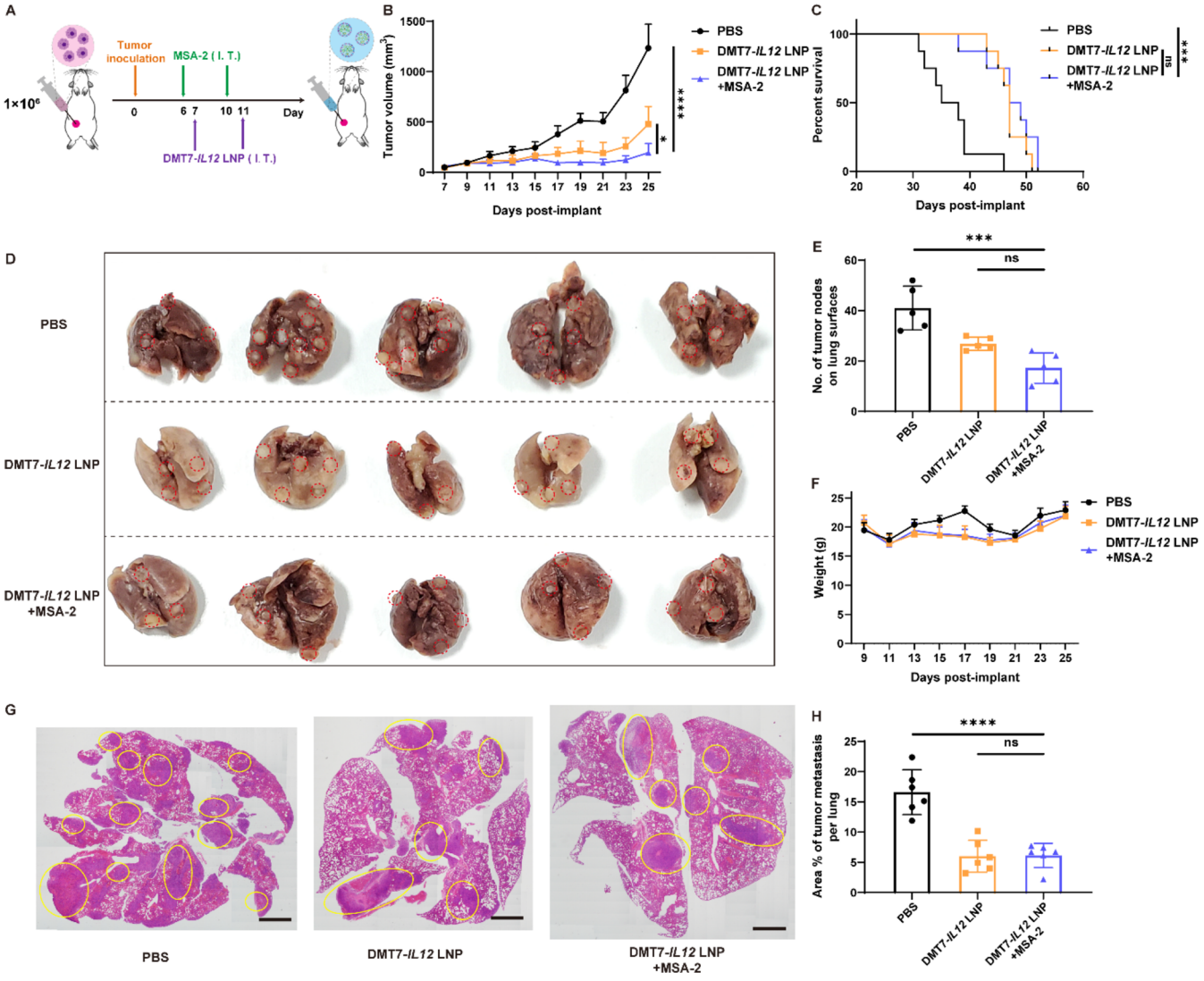

Figure 5. In vivo evaluation of antitumor activity of DMT7-*IL12* LNP with MSA-2 in the 4T1 breast cancer model. (A) Schematic representation of the administration strategy. (B) Average tumor growth curves of mice bearing 4T1 tumors and subjected to different therapeutic combinations (n = 8). (C) Kaplan−Meier survival curves for the mice. Statistical significance was determined using the log-rank test. (D) Changes in body weight following intratumoral administration of different treatment groups. (E) Representative images of lungs after treatments with the indicated combinations. (F) Quantification of metastatic foci on the lung surfaces from (E) (n = 6). (G) Representative H&E-stained lung sections, scale bar, 2 mm. (H) Percentage of tumor area within the total lung area after treatments with different combinations (n = 6). Significant differences were assessed using a one-way ANOVA with Tukey's test for (B, F, and H). The level of significance is indicated as follows: $p > 0.05$ (ns, not significant), *$p < 0.05$, ***$p < 0.001$, and ****$p < 0.0001$. All data in (B, F, and H) are presented as mean ± SD.

+ MSA-2 treatment, our next objective was to explore the potential enhanced antitumor effect of this combinatorial approach. In the contralateral B16F10 dual-tumor model, it was observed that tumors grew rapidly in the groups treated with PBS and blank DMT7 LNPs (Figure 4B). Unfortunately, all tumor-bearing mice succumbed to the disease within 30 days, indicating the aggressiveness of the tumor growth in these untreated and control groups (Figure 4C). As shown in Figure 4B, DMT7-*IL12* LNP + MSA-2 demonstrated a notably potent antitumor effect on the treated tumor sides, leading to a 74.5% reduction in tumor volume compared to DMT7-*IL12* LNP treatment alone. Moreover, this combinatorial treatment

https://doi.org/10.1021/acsnano.4c00063
ACS Nano 2024, 18, 15499−15516

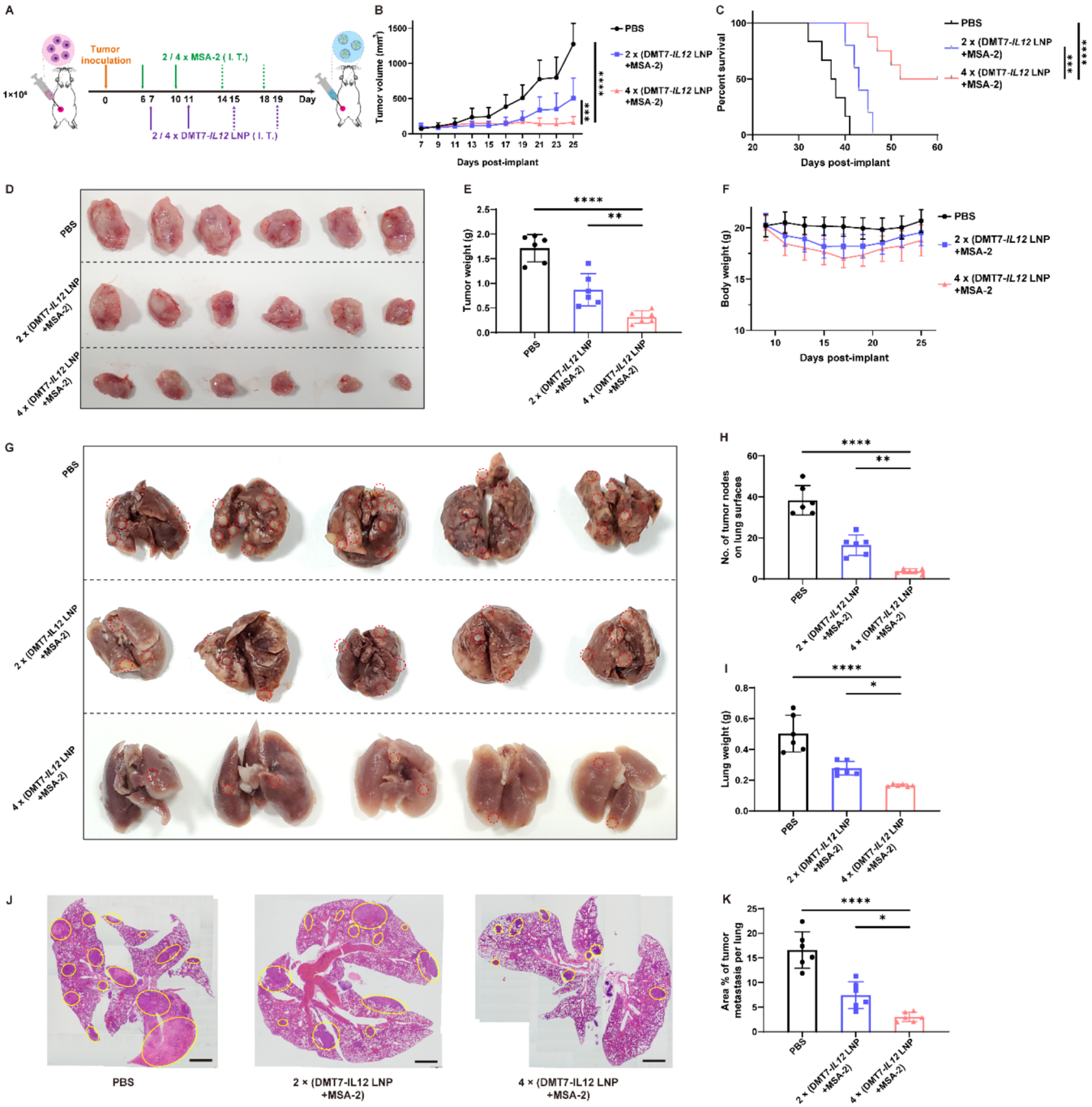

Figure 6. Antitumor activity of doubling treatment cycles of DMT7-*IL12* LNP + MSA-2 in the 4T1 breast cancer model. (A) Schematic representation of the antitumor treatment regimen. (B, C) Average tumor growth curves (B) and Kaplan−Meier survival curves (C) of 4T1 tumor-bearing mice treated with various therapeutic combinations. (D, E) Representative images (D) and weights (E) of excised 4T1 tumors (n = 6−8). (F) Changes in body weight following intratumoral administration of the indicated treatment groups. (G−I) Representative images of lungs (G), lung weights (H), and the number of metastatic foci on lung surfaces (I) after treatment with different combinations. (J) Representative lung sections stained with H&E, scale bar, 2 mm. (K) Percentage of tumor area within the total lung area following treatment (n = 6). Significant differences were evaluated using a one-way ANOVA with Tukey's test for (B, E, H, I, and K). The significance levels are as follows: *p < 0.05, **p < 0.01, ***p < 0.001, and ****p < 0.0001. The statistical significance of the survival curve was determined using the log-rank test (C). Data in (B, E, F, H, I, and K) are presented as mean ± SD.

significantly prolonged the overall survival of tumor-bearing mice for over 2 months, with an improved cure rate of 50%. We also monitored the growth of untreated tumors on the contralateral side. Notably, enhanced tumor regression was observed after treatment with DMT7-*IL12* LNP + MSA-2, while moderate tumor growth inhibition was observed in the DMT7-*IL12* LNP, blank DMT7 LNP, or PBS-treated groups. Collectively, these results suggest that the combination of DMT7-*IL12* LNP with MSA-2 enhances the antitumor effect and demonstrates durable antitumor immunity.

Using the dosing strategy described in Figure 4I to assess the impact of DMT7-*IL12* LNP + MSA-2 on immune cell

https://doi.org/10.1021/acsnano.4c00063
ACS Nano 2024, 18, 15499−15516

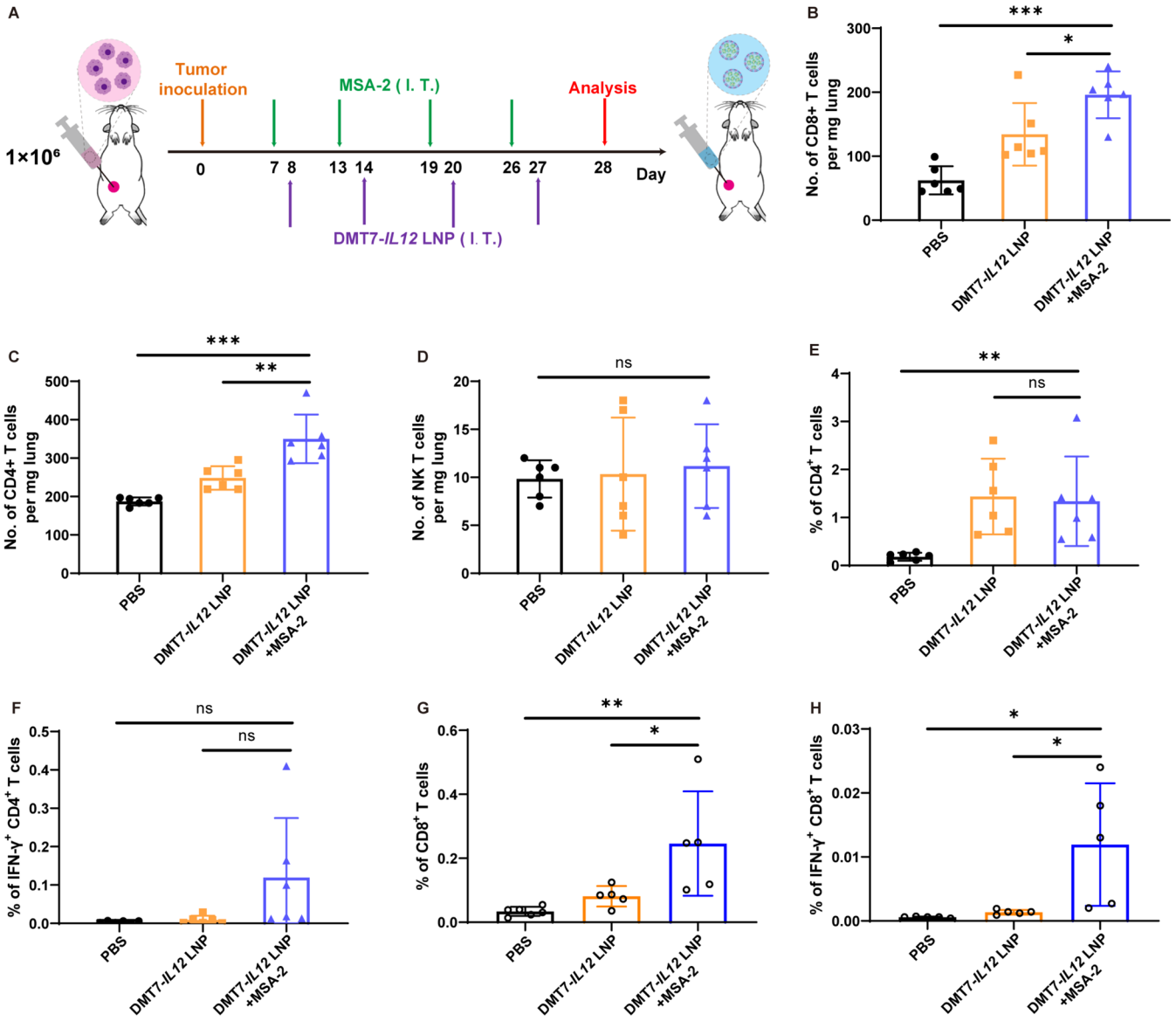

Figure 7. (A) Schematic representation of the treatment regimen for flow cytometry analysis. (B−D) Flow cytometry analysis of immune cell subsets in the lungs of mice treated with different combinations: (B) CD8+ T cells, (C) CD4+ T cells, and (D) NK T cells. (E−H) Flow cytometry analysis of immune cell subsets in the serum of mice from different treatment groups: (E) CD4+ T cells, (F) IFN-γ + CD4+ T cells, (G) CD8+ T cells, and (H) IFN-γ + CD8+ T cells (n = 6). All significant differences were assessed using a one-way ANOVA with the Tukey test. The level of significance is indicated as follows: $p > 0.05$ (ns, not significant), *$p < 0.05$, **$p < 0.01$, and ***$p < 0.001$. Data in (B−H) are presented as mean ± SD.

infiltration within TME, we conducted an analysis 24 h after the final administration of the different formulations. Notably, in comparison to the groups treated with PBS and blank DMT7 LNPs, the DMT7-*IL12* LNP + MSA-2 treatment group exhibited a significant increase in the count of tumor-infiltrating CD4+ T helper and CD8+ T effector cells. Notably, the level of CD8+ T effector cells was increased by 2.75-fold compared to that observed in the DMT7-*IL12* LNP group (Figure 4J,K). DMT7-*IL12* LNP + MSA-2 treatment also increased the recruitment of NK cells and granulocytes by 2.75- and 4.8-fold, respectively, compared to the DMT7-*IL12* LNP treatment group. These findings underscore the potent effect of DMT7-*IL12* LNP + MSA-2 in promoting the infiltration and activation of immune cells in the TME. The infiltrated regulatory T cells (Treg) decreased by 19 and 29%, respectively, following treatment with DMT7-*IL12* LNP or DMT7-*IL12* LNP + MSA-2 compared to the PBS treatment group (Figure 4L). Moreover, the administration of DMT7-*IL12* LNP + MSA-2 not only augmented the infiltration of immune cells but also promoted the polarization of macrophages from the immunosuppressive M2 state toward the immunostimulatory M1 phenotype, compared to the other treatment groups (Figure 4M). These findings suggested that the combined strategy of MSA-2 and DMT7-*IL12* LNP was effective in reprogramming the immunosuppressive environment in tumors. Additionally, we assessed the levels of IL-12, TNF-α, and IFN-γ, important indicators of effector T cell activity and proliferation. Compared with the PBS or blank DMT7 LNP group, IL-2, and TNF-α levels in the DMT7-*IL12* LNP + MSA-2 treatment group were increased by 3.12- and 1.48-fold, respectively (Figure 4O−P). DMT7-*IL12* LNP + MSA-2 treatment further revealed the activation of antitumor

https://doi.org/10.1021/acsnano.4c00063
ACS Nano 2024, 18, 15499−15516

immune responses and effector functionality recovery of T cells, as evidenced by the improved levels of IFN-γ (2−6.3-fold) and IL-12 (3.1−3.5-fold) either in TME or in circulation system as compared to PBS and blank DMT7 treatment groups (Figures 4N,Q and S28). Overall, DMT7-*IL12* LNP + MSA-2 induced extensive infiltration of immune cells within TME and triggered a robust and effective antitumor immune response.

Suppressed Tumor Growth with DMT7-*IL12* LNP in the Presence of MSA-2 in the 4T1 Tumor Model. Since DMT7-*IL12* LNP + MSA-2 significantly inhibited tumor growth at the untreated side in a contralateral B16F10 dual-tumor model, it is essential to assess the systemic immunotherapy efficacy of DMT7-*IL12* LNP + MSA-2. The systemic antitumor effect of this treatment was evaluated in a mouse model bearing 4T1 lung metastases via intratumoral injection of DMT7-*IL12* LNP + MSA-2 (Figure 5A). The data revealed that DMT7-*IL12* LNP + MSA-2 significantly suppressed the growth of primary 4T1 tumors, resulting in a 40.5% reduction in tumor volume compared with the DMT7-*IL12* LNP treatment group (Figure 5B). However, our analysis revealed no significant difference in the median survival time of animals treated with either DMT7-*IL12* LNP alone or in combination with MSA-2 (Figure 5C). Lung tissues were isolated and processed for hematoxylin and eosin (H&E) staining on day 30 postinoculation. As shown in Figure 5D,E, when compared to the PBS-treated group, DMT7-*IL12* LNP treatment significantly reduced the number of tumor nodules on the lung surfaces by 45.4%, while the combination of DMT7-*IL12* LNP and MSA-2 demonstrated an even more profound reduction of 76.9%. In terms of the relative area of metastases within the lungs, both DMT7-*IL12* LNP and DMT7-*IL12* LNP + MSA-2 inhibited the growth of 4T1 metastases by 37.5 and 55% over the PBS treatment group (Figure 5G,H). However, no notable difference in the antimetastasis ability was observed between the DMT7-*IL12* LNP and DMT7-*IL12* LNP + MSA-2 treatment groups. These results further support the notion that DMT7-*IL12* LNP + MSA-2 exhibits systemic immunotherapy efficacy similar to that of DMT7-*IL12* LNP alone. Collectively, the 4T1 lung metastases model exhibited a diminished therapeutic response toward MSA-2, leading to an impaired recruitment efficiency of nonexhausted T cells into the tumors, thereby restricting the overall antitumor immune response.

Impact of Treatment Frequency of DMT7-*IL12* LNP + MSA-2 on the Antitumor Efficacy in the 4T1 Tumor Model. In terms of the slightly intensified antitumor activity observed with DMT7-*IL12* LNP + MSA-2 therapy in both primary tumor sites and distal lung metastases compared with DMT7-*IL12* LNP treatment, we aimed to determine whether doubling the treatment frequency of DMT7-*IL12* LNP + MSA-2 could achieve a better antitumor ability in the 4T1 lung metastases model. Using the treatment strategy described in Figure 6A, 4T1 tumor-bearing mice were intratumorally treated with two or four injections of MSA-2 combined with DMT7-*IL12* LNP at multiple time points. According to the results in Figure 6, both the administration of 2 × (DMT7-*IL12* LNP + MSA-2) and 4 × (DMT7-*IL12* LNP + MSA-2) significantly enhanced the regression of primary tumors and distal metastases compared with the PBS treatment group. Interestingly, treatment with 4 × (DMT7-*IL12* LNP + MSA-2) inhibited primary tumor growth, resulting in a 56.5% reduction in tumor volume compared to the 2 × (DMT7-*IL12* LNP + MSA-2) treatment group (Figure 6B,D,E). Additionally, the 4 × (DMT7-*IL12* LNP + MSA-2) treatment group prolonged overall animal survival, accompanied by an improved cure rate of 50% (Figure 6C). Furthermore, we found that compared with PBS and 2 × (DMT7-*IL12* LNP + MSA-2) treatment groups, the number of tumor nodules on the lung surfaces in the 4 × (DMT7-*IL12* LNP + MSA-2) treatment group was significantly reduced by 89.5 and 77.8%, respectively, suggesting that multiple treatment frequencies are necessary for achieving enhanced tumor inhibition in a 4T1 lung metastases model (Figure 6G,H). Similarly, 4 × (DMT7-*IL12* LNP + MSA-2) treatment decreased lung weight and the relative area of metastases within the lungs compared to PBS and 2 × (DMT7-*IL12* LNP + MSA-2) treatment groups (Figure 6I,K). The results indicate that increasing the treatment frequency of DMT7-*IL12* LNP + MSA-2 leads to more effective antitumor activity in the mouse model of lung metastases. These findings offer valuable insights for optimizing DMT7-*IL12* LNP + MSA-2 therapy and achieving improved outcomes in various preclinical tumor models.

To further elucidate the immunotherapeutic mechanism of DMT7-*IL12* LNP + MSA-2 therapy in the 4T1 lung metastases model, we performed flow cytometry analysis to investigate its influence on immune cell infiltration within the lungs (Figure 7A). After administering DMT7-*IL12* LNP + MSA-2, we did not detect any notable differences in the infiltration of NK T cells into the lungs (Figure 7D). However, a statistically significant elevation in the frequencies of CD8+ and CD4+ T cells was evident in the group treated with DMT7-*IL12* LNP + MSA-2, compared to both the DMT7-*IL12* LNP and PBS treatment groups (Figure 7B,C). Furthermore, to investigate the potential systemic antitumor immunity elicited by intratumoral injections of DMT7-*IL12* LNP + MSA-2 at the primary tumor site, mouse serum was harvested from mice bearing 4T1 tumors 28 days after tumor inoculation and then subjected to analysis using flow cytometry. No notable difference in the average levels of CD4+ and IFN-γ + CD4+ T cells in serum was observed between the DMT7-*IL12* LNP and DMT7-*IL12* LNP + MSA-2 treatment groups (Figure 7E,F). However, the administration of DMT7-*IL12* LNP + MSA-2 elevated the average levels of CD8+ and IFN-γ + CD8+ T cells in serum compared to DMT7-*IL12* LNP alone (Figure 7G,H). Both the DMT7-*IL12* LNP + MSA-2 and DMT7-*IL12* LNP treatments led to a significant increase in the proportion of CD8+ and CD4+ T cells in the serum compared to the PBS treatment group (Figure 7E,G). Collectively, intratumoral administrations of DMT7-*IL12* LNP + MSA-2 dynamically integrated STING agonist-mediated innate immune stimuli with IL-12-mediated adaptive immune stimuli to generate a robust systemic antitumor immunity while reducing T cell exhaustion, effectively preventing tumor metastases in a 4T1 lung metastases model.

Improved Antitumor Activity of DMT7-*IL12* LNP + MSA-2 Therapy with αPD-1 in Both B16F10 and 4T1 Mouse Tumor Models. The previous results strongly support the effectiveness of DMT7-*IL12* LNP + MSA-2 therapy as a highly promising avenue in the field of cancer immunotherapy. The PD-1 inhibitory pathway plays a crucial role in regulating T cell exhaustion during cancer progression.[36] In the past few years, PD-1-targeting agents have been widely used as first-line antitumor therapeutics in the clinic. Nonetheless, not all patients exhibit a favorable response to αPD-1 monotherapy,

https://doi.org/10.1021/acsnano.4c00063
ACS Nano 2024, 18, 15499−15516

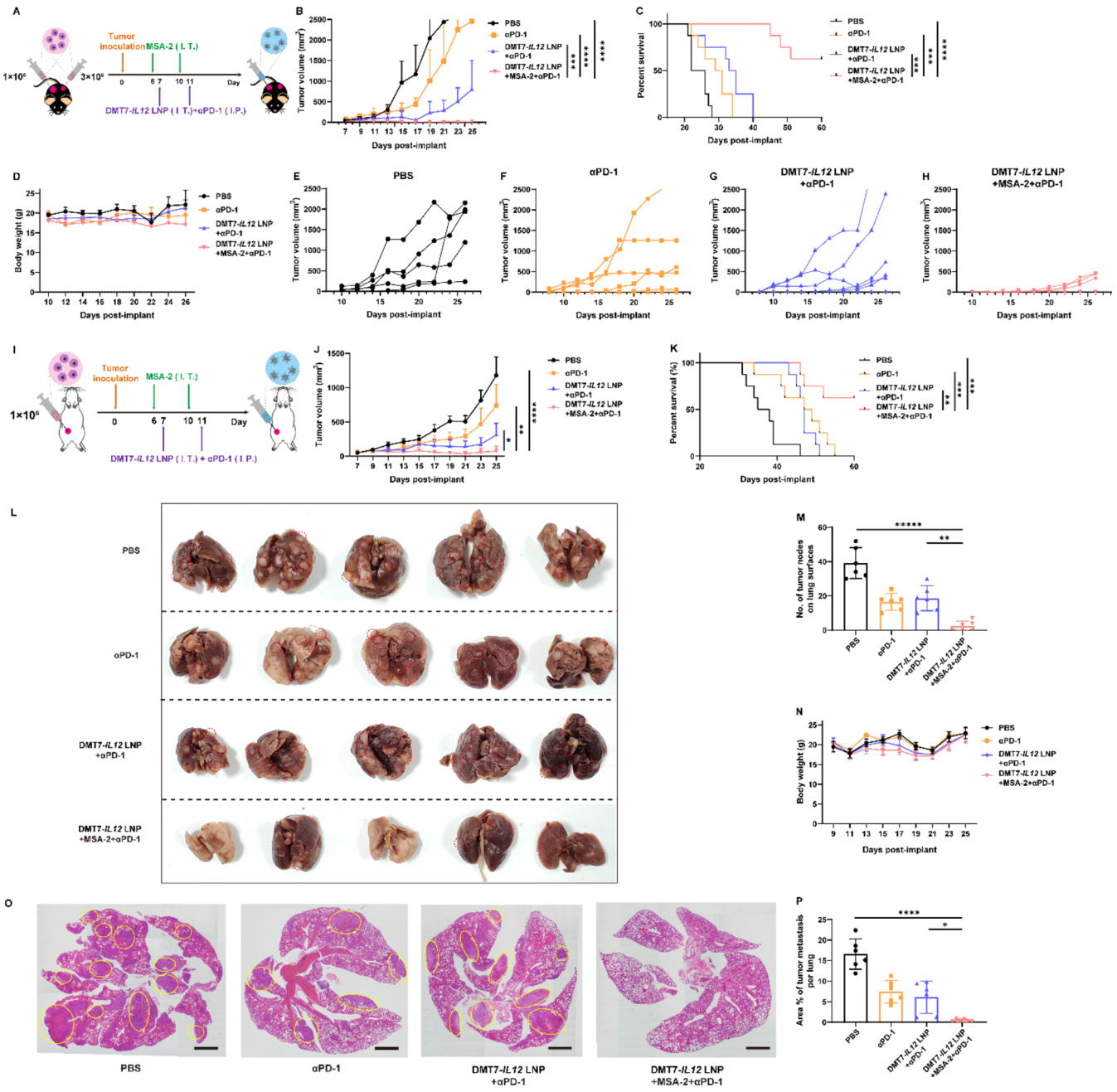

Figure 8. In vivo evaluation of antitumor activity of DMT7-*IL12* LNP + MSA-2 with αPD-1. (A) Schematic representation of the treatment regimen for anti-B16F10 tumor study. (B, C) Analysis of mice bearing B16F10 melanoma treated with different therapeutic combinations, showing average tumor growth (B) and Kaplan−Meier survival curves (C). (D) Monitoring of body weight changes following intratumoral administration of the specified treatment groups. (E−H) Tumor volumes of individual mice on the untreated side (n = 5−8). (I) Schematic representation of the treatment protocol for the anti-4T1 tumor study. (J, K) Evaluation of 4T1 tumor-bearing mice treated with various therapeutic combinations, revealing average tumor growth (J) and Kaplan−Meier survival curves (K). (L, M) Representative images (L) of lungs and quantification of metastatic foci (M) on lung surfaces following treatment with different therapeutic combinations. (N) Monitoring of body weight changes following intratumoral administration of the designated treatment groups. (O) Representative lung sections stained with H&E, scale bar, 2 mm. (P) Quantification of the percentage of tumor area relative to the total lung area following treatments (n = 6). Significant differences were determined using a one-way ANOVA with Tukey's test for (B, J, M, and P). The statistical significance of survival curves was evaluated using the log-rank test for (C, K). Data presented in (B, D, J, M, N, and P) represent the mean ± SD from the second experiment. Significance levels are indicated as follows: *p < 0.05, **p < 0.01, ***p < 0.001, and ****p < 0.0001.

implying that the reversal of T cell exhaustion cannot solely depend on the elimination of the PD-1 inhibitory brake, but it is also imperative to provide stimulatory signals to T cells to effectively overcome exhaustion and promote a robust antitumor immune response. This led us to combine PD-1 blockade with DMT7-*IL12* LNP + MSA-2 therapy as a strategy to further improve the overall response rate across multiple tumor models.

As depicted in Figure 8A,I, tumor-bearing mice were concurrently administered systemic αPD-1 therapy, replicating a clinical setting where immune checkpoint blockade (ICB) inhibitors are employed as the standard of care.[37] We first

https://doi.org/10.1021/acsnano.4c00063
ACS Nano 2024, 18, 15499−15516

investigated the antitumor activity of DMT7-*IL12* LNP + MSA-2 with αPD-1 in a contralateral B16F10 dual-tumor model. As shown in Figure 8B,C,F, αPD-1 alone caused a moderate antitumor efficacy in both treated and untreated tumors. The combined DMT7-*IL12* LNP + αPD-1 treatment resulted in a significant enhancement of antitumor activity and overall survival when compared to the PBS treatment group (Figure 8B,C,G). Furthermore, when compared to other treatment groups, a complete tumor regression (Figure 8B,H) and a durable cure rate of 65% (Figure 8C) were observed after treatment with DMT7-*IL12* LNP + MSA-2 + αPD-1. This suggests that the antitumor activity of DMT7-*IL12* LNP + MSA-2 therapy is significantly boosted by αPD-1. Next, we evaluated the combination of intratumoral DMT7-*IL12* LNP + MSA-2 and αPD-1 in a 4T1 lung metastases model. With the addition of αPD-1, DMT7-*IL12* LNP + MSA-2 treatment significantly improved the therapeutic efficacy in primary tumors (Figure 8J), leading to prolonged median survival of 4T1 tumor-bearing mice and an improved cure rate of 65% compared to other treatment groups (Figure 8K). Moreover, the addition of αPD-1 to DMT7-*IL12* LNP + MSA-2 treatment dramatically reduced the number of tumor nodules on the lung surfaces. No detectable metastases were observed even 30 days after tumor inoculation compared to other treatment groups (Figure 8O,P). The significant reduction in tumor nodules and absence of metastases can be attributed to the synergistic effect of reinforced systemic antitumor immunity achieved by the inclusion of αPD-1 in the treatment regimen. In summary, the combination of DMT7-*IL12* LNP + MSA-2 and αPD-1 showed superior inhibition of both primary and distal tumor growth compared to each therapy alone. This highlights the potential of this combination as a powerful therapeutic strategy to enhance the overall antitumor immune response.

Biodistribution and Toxicity Assessment of DMT7 LNP. To further investigate the biodistribution of DMT7 LNP, we labeled it with Cy7 (Cy7-DMT7 LNP) and observed that it accumulated significantly at the tumor site for 96 h, with no discernible fluorescence signal detected in other organs (Figures S29 and S30). The blood levels of DMT7 LNP peaked at 24 h postinjection but rapidly cleared within the next 72 h (Figure S31), indicating its efficient biodegradation. There was no evidence of inflammation following intratumoral administration of the blank DMT7 LNP, as determined by flow cytometry analysis of immune cells in the TME (Figure 4J,K), indicating the low immunogenicity of DMT7 LNP. Furthermore, throughout the entire treatment period for all in vivo studies, no notable weight loss or behavioral alterations were observed in any of the animals.

The potential adverse effects of DMT7 LNP were further evaluated through hematological assessment and histological examination. H&E staining revealed no pathological changes in major organs (heart, liver, spleen, lung, and kidney) after two intratumoral administrations of empty DMT7 LNP (Figure S32). To further assess the organ function (heart, liver, and kidney), serum levels of biochemical indicators such as alanine aminotransferase (ALA), low-density lipoprotein cholesterol (LDL-c), aspartate transaminase (AST), creatine kinase (CK), blood urea nitrogen (BUN), and creatinine were measured. Comparable to the PBS groups, the levels of these indicators in mice treated with DMT7 LNP remained within the reference ranges (Figure S33), suggesting that LNP treatment did not induce notable cardiac, hepatic, or renal toxicity. These results confirm the excellent biocompatibility of DMT7 LNP, suggesting its safety for further development as LNP-based mRNA nanomedicine for cancer therapy or viral infectious diseases.

DISCUSSION

STING agonists play a vital role in promoting tumor-reactive T cell trafficking into the TME, which is crucial for antitumor immunity.[38,39] However, while STING agonists have shown successful therapeutic effects against early-stage solid tumors, the response to treatment varies significantly among patients, and the clinical outcomes have been less than satisfactory due to immunosuppression in many tumor types.[40] In this study, we observed a similar phenomenon that treatment with MSA-2, a potent STING agonist,[2] could only prevent tumor growth at the early stages of tumor progression without inducing a continuous antitumor immune response. T cell exhaustion, characterized by a gradual decline in effector function and persistent expression of inhibitory receptors, most likely explains the unsatisfactory efficacy of STING agonist-based cancer therapy. Therefore, reversing T cell exhaustion to enhance antitumor immunity is a crucial component for successful immunotherapy. Currently, multiple strategies have been investigated to restore exhausted T cell functions. One approach to enhancing antitumor therapy effectiveness in gliomas and glioblastomas involves restoring normoxia, which has demonstrated its effectiveness in mitigating CD8+ T cell exhaustion.[41,42] Another approach involves the use of *N*-acetylcysteine, a known antioxidant and ROS scavenger, which acts directly on T cell metabolism to enhance mitochondrial function and successfully restore T cell function in vitro and in vivo.[43] Additionally, the inclusion of immunostimulants, such as the administration of IL-2, could also reverse T cell exhaustion and facilitate additional immune system mechanisms to drive tumor suppression.[44] Unfortunately, none of these approaches have been clinically approved to address the challenges associated with T cell exhaustion, highlighting an unmet demand for alternative solutions. Here, we present a promising candidate for combination therapy with MSA-2 and IL-12, aiming at in situ modulation of the TIME and restoration of complete effector functionality in T cells. The rationale for this approach lies in two key aspects: first, to facilitate the infiltration of fresh, nonexhausted T cells into the TME through the MSA-2-mediated innate immune response; second, to concurrently deliver a stimulatory signal to T cells via IL-12, a potent driver of CD8+ T cell effector functions and prevention against CD8+ T cell exhaustion.[45−47]

Given the limited bioavailability and short plasma half-life of recombinant cytokine IL-12, using mRNA technology to induce the sustained local expression of bioactive IL-12 within the TME is a relevant solution. mRNA nanomedicine, as an emerging biotechnology platform, offers opportunities for preventing and treating various clinical indications. The outstanding effectiveness of COVID-19 mRNA vaccines has recently generated intense studies, leading to the design and development of innovative LNP-based mRNA delivery systems for cancer immunotherapy.[23,48,49] LNP-based nanocarriers have the potential for prolonged and local delivery of IL-12, providing an ideal alternative to overcome the toxicity associated with systemic administration.[24,50] Although mRNA-based drugs have made progress in translational research, few mRNA nanomedicines (mRNA vaccines or therapies) have been applied to cancer therapy in the clinic

https://doi.org/10.1021/acsnano.4c00063
ACS Nano 2024, 18, 15499−15516

until recently. The primary concern lies in the safety and efficiency issues associated with the delivery platforms. To tackle this challenge, we created and synthesized a series of ionizable amino lipids, subsequently formulating them into LNPs for efficient mRNA delivery. Our developed DMT7 LNP not only exhibits a higher mRNA delivery efficiency compared to commercial ALC-0315 LNP in vivo but also shows no discernible harm to major organs or impairment of heart, liver, and kidney function following intratumoral administration. Therefore, it could be a potentially effective and safe mRNA delivery platform for in situ vaccination of tumors.

As expected, the combinatorial approach using DMT7-*IL12* LNP and MSA-2 showed great efficacy in reversing the exhausted phenotype of T cells. This was characterized by their impaired production of effector cytokines and high levels of inhibitory receptors. The combination of DMT7-*IL12* LNP + MSA-2 therapy significantly boosted cytokine production (IFN-γ, TNF-α, and Granzyme B) in tumor-infiltrating CD8+ T cells. Furthermore, the combined therapy of DMT7-*IL12* LNP + MSA-2 notably reduced the expression levels of inhibitory molecules such as TIM-3 and PD-1 on these cells when compared to control groups receiving MSA-2 or DMT7-*IL12* LNP as monotherapy. These findings suggest that the combination therapy potentiates antitumor immune responses by reinvigorating CD8+ T cells. In a contralateral B16F10 dual-tumor model, this combination treatment resulted in a 74.5% reduction in tumor volume, as compared to the treatment with DMT7-*IL12* LNP alone. This treatment also increased the generation of CD8+ and CD4+ T cells, promoting their secretion of proinflammatory cytokines (TNF-α, IL-2, IFN-γ, and IL-12) in B16F10 tumor tissues. The antitumor effect of DMT7-*IL12* LNP + MSA-2 therapy was further assessed in a 4T1 lung metastases model. This treatment demonstrated a comparable ability to inhibit tumor growth in both primary tumors and distal tumor metastases when compared to DMT7-*IL12* LNP treatment alone. Given that 4T1 tumors exhibited a reduced therapeutic response to MSA-2, it is possible that the prescribed treatment frequency may result in suboptimal responses or even treatment failure in various cancer types. Therefore, it is essential to consider the optimal treatment frequency for each cancer type to ensure optimal therapeutic outcomes. We therefore investigated whether doubling the treatment frequency of DMT7-*IL12* LNP + MSA-2 could enhance its antitumor efficacy. Surprisingly, 4× (DMT7-*IL12* LNP + MSA-2) treatment significantly suppressed the growth of both primary and distant tumor metastases compared to 2× (DMT7-*IL12* LNP + MSA-2). This significant reduction in tumor volume was presumably attributed to the elevated frequencies of CD8+ and CD4+ T cells producing IFN-γ in the serums and lungs of mice with 4T1 tumors. To further enhance the antitumor efficacy of DMT7-*IL12* LNP + MSA-2 therapy, we added αPD-1 to the treatment protocol. Despite the absence of a significant difference in the median survival time between the animals treated with DMT7-*IL12* LNP + MSA-2 and those receiving DMT7-*IL12* LNP + MSA-2 in combination with aPD-1, it is noteworthy that both treatments demonstrated therapeutic efficacy. Notably, the combined therapy utilizing DMT7-*IL12* LNP + MSA-2 along with αPD-1 led to nearly complete responses, not only in the directly treated tumors but also in distal, untreated tumors and metastases. These profound findings highlight the treatment's ability to elicit potent systemic antitumor immunity in vivo, suggesting its promise as a potential therapeutic approach.

Preclinical studies that exclusively focused on IL-12 delivery often reported therapeutic efficacy limited to the treatment of small tumor burdens. This limitation is presumably attributed to the insufficient stimulation of all aspects of the cancer-immunity cycle by a single cytokine, as well as the compromised effector function of T cells within larger tumor tissues.[51,52] So far, no studies have specifically examined the potential synergistic effect of IL-12 coupled with STING agonists in reversing T cell exhaustion. Our developed combination immunotherapy strategy, which enhances the activation, proliferation, and survival of immune cells while reversing the exhausted phenotype of T cells, promoting immune rejection of tumors by harnessing the immunoregulatory function of both IL-12 and the STING pathway, has demonstrated superior antitumor efficacy compared to treatment with MSA-2 or DMT7-*IL12* LNP alone. Furthermore, the strategy proposed in this research has significant implications for clinical trials, as DMT7-*IL12* LNP + MSA-2 could be combined with αPD-1, which has already undergone clinical evaluation. For future studies, it is essential to conduct a comprehensive investigation regarding the impact of the dosing strategy and treatment frequency of DMT7-*IL12* LNP or MSA-2 on the antitumor effect, providing valuable insights for optimizing the treatment regimen. Additionally, in the translational research setting, a thorough assessment of the pharmacokinetics and toxicology profiles of DMT7-*IL12* LNP or MSA-2 following intratumoral administration is crucial. These evaluations will inform and guide the potential clinical translation of this approach, ensuring its safety and efficacy in clinical trials. Furthermore, we aim to develop LNPs with tumor-targeting capabilities and investigate their antitumor efficacy in orthotopic tumors through systemic administration.

CONCLUSIONS

In summary, our study presents a robust combination immunotherapy strategy designed to restore the exhausted phenotype of T cells for improved cancer immunotherapy. By combining MSA-2-induced STING activation with local delivery of IL-12 in the tumor microenvironment using DMT7-*IL12* LNP, we successfully rejuvenated the immunosuppressive tumor immune microenvironment and reversed the exhausted phenotype of T cells in the tumor. This resulted in significantly improved antitumor efficacy in both established B16F10 and 4T1 tumor models. This innovative combinatorial approach presents a proof of concept for effectively and safely addressing T cell exhaustion in the realm of cancer immunotherapy.

EXPERIMENTAL SECTION

Materials. pVAX1-*IL12* plasmid was obtained from Suzhou Genewiz Biotechnology Co., Ltd. (China). Trypsin-EDTA, penicillin–streptomycin solution, RPMI 1640 medium, FBS, and Dulbecco's modified Eagle's medium (DMEM) were purchased from Gibco (USA). Kanamycin and ammonium sulfate were acquired from Shanghai Aladdin Bio-Chem Technology Co., Ltd. (China). Cy7-labeled cholesterol was obtained from Sigma-Aldrich Co., Ltd. (USA). All agents not specified were acquired from Sigma-Aldrich unless otherwise noted.

To assess the morphology of lipid nanoparticles (LNPs), a transmission electron microscope (TEM) from Thermo Scientific (Talos, Waltham, MA) was utilized. Furthermore, dynamic light scattering (DLS, Malvern, Worcestershire) measurements were

https://doi.org/10.1021/acsnano.4c00063
ACS Nano 2024, 18, 15499−15516

conducted to determine the average particle size and ζ-potential of the LNPs.

Cell Lines and Animals. B16F10 and 4T1 cells (ATCC) were cultured in RPMI 1640 medium supplemented with 10% FBS. Female C57BL/6 or Balb/c mice were sourced from Charles River Laboratories (Beijing). All animal experiments conducted in this study complied with the ethical standards and guidelines established by the Animal Care and Use Committee of Shanghai Jiao Tong University.

mRNA Design, Synthesis, and Formulation. Secreted IL-12 was designed using the native nucleotide sequences encoding the protein subunits IL-12B and IL-12A, also known as IL-12 p40 and IL-12 p30, respectively. For mice, the reference sequences are NM_001303244 (IL-12B) and NM_031252 (IL-12A). These sequences were merged into a single construct with a linker bridging the IL-12B and IL-12A subunits. The signal peptide of IL-12B was preserved to facilitate secretion, while the signal peptide of IL-12A was excised (corresponding to the first 21 amino acids in mice and 19 amino acids in humans, as per the UniProt entries Q9EQ14 for mouse and Q9NPF7 for human). Firefly luciferase mRNA (*FLuc* mRNA), green fluorescence protein mRNA (*GFP* mRNA), and interleukin-12 mRNA (*IL12* mRNA) were synthesized in vitro using the T7 RNA polymerase transcription method. This process involved the use of a linearized DNA template that incorporated the 5′ and 3′ untranslated regions (UTRs) and a polyadenylated tail, as described previously.[19] Additionally, uridine 5′-triphosphate (UTP) was replaced with N1-methylpseudo UTP during transcription. Furthermore, a Cap1-GAG analogue was employed to enhance the translation efficiency of the mRNA. The size and sequence of these mRNAs are provided in Table S3.

Synthesis of Different Ionizable Amino Lipids. $CDCl_3$, DMSO-d_6, or CD_3OD served as the solvent, and the internal standard was trimethylsilane (TMS). Mass spectrometry was performed on a Finnigan MAT-95/711 spectrometer. Thin-layer chromatography (TLC) analyses were conducted on Merck silica gel 60 F_{254} plates. The solvents used were $CDCl_3$, DMSO-d_6, or CD_3OD, with trimethylsilane (TMS) serving as the internal standard. The synthesized compounds were identified through proton nuclear magnetic resonance (^{1}H NMR) on a Bruker AMX-400 spectrometer. The corresponding results are illustrated in Figures S5−S15.

The synthesis of (9*Z*,12*Z*)-octadeca-9,12-dien-1-ol (Compound b), (9*Z*,12*Z*)-octadeca-9,12-dien-1-yl methanesulfonate (Compound c), (6*Z*,9*Z*)-18-bromooctadeca-6,9-diene (Compound d), and (6*Z*,9*Z*,28*Z*,31*Z*)-heptatriaconta-6,9,28,31-tetraen-19-ol (Compound e) followed the protocol as described previously.[53,54]

(6*Z*,9*Z*,28*Z*,31*Z*)-Heptatriaconta-6,9,28,31-tetraen-19-yl 3-Bromopropanoate (Compound f). Triethylamine (0.50 g, 4.92 mM) and Compound e (2.0 g, 3.78 mM) were dissolved in anhydrous THF (20 mL) and stirred at 0 °C for 30 min under nitrogen. Subsequently, bromopropionyl chloride (0.98 g, 4.54 mM) was added dropwise. Following the reaction and purification via column chromatography, Compound f, was obtained in its pure form as a colorless oil (2.1 g, 83.7%).

(6*Z*,9*Z*,28*Z*,31*Z*)-Heptatriaconta-6,9,28,31-tetraen-19-yl 3-(4-(2-hydroxyethyl) Piperazin-1-yl) Propanoate (Ionizable Lipid Compound HPZE1). Compound f (0.5 g, 0.75 mM), *N*,*N*-diisopropylethylamine (DIPEA, 0.15 g, 1.13 mM), 2-(piperazin-1-yl) ethan-1-ol (0.18 g, 0.90 mM), and 5 mL of anhydrous ethanol were added to the reaction flask. Following the reaction and purification via column chromatography, compound HPZE1 was obtained in its pure form as a colorless oil (57.7%). The synthetic route of HPZE1 is described in Figure S1, and ionizable amino lipids HPZE2, HPZE3, and HPDE4 can be synthesized using the same method described above.

(6*Z*,9*Z*,28*Z*,31*Z*)-Heptatriaconta-6,9,28,31-tetraen-19-yl (2-(4-Methylpiperazin-1-yl) ethyl) Carbamate (Ionizable Lipid Compound HPZC5). Compound e (0.5 g, 0.95 mM), *N*,*N*′-disuccinimidyl carbonate (0.29 g, 1.13 mM), and anhydrous DCM (5 mL) were combined in the reaction flask. Subsequently, 2-(4-methylpiperazin-1-yl) ethan-1-amine (0.16 g, 1.13 mM) was added, and following the reaction and purification via column chromatography, compound HPZC5 was obtained in its pure form as a colorless oil (0.52 g, 78.8%). The synthetic route of HPZC5 is described in Figure S2, and ionizable amino lipid HPZC6 can be synthesized using the same method described above.

2-((6*Z*,9*Z*,28*Z*,31*Z*)-Heptatriaconta-6,9,28,31-tetraen-19-yl) Isoindoline-1,3-dione (Compound g). Triphenylphosphine (3.22 g, 12.29 mM), Compound e (5.0 g, 9.45 mM), phthalimide (1.7 g, 11.34 mM), and diethyl ether (50 mL) were combined in the reaction flask. Diisopropyl azodicarboxylate (1.8 g, 12.29 mM) was then added dropwise. Following the reaction and purification via column chromatography, Compound g was obtained in its pure form as a colorless oil (5.5 g, 88.4%).

(6*Z*,9*Z*,28*Z*,31*Z*)-Heptatriaconta-6,9,28,31-tetraen-19-amine (Compound h). Compound g (3.0 g, 4.56 mM) was dissolved in diethyl ethanol (20 mL), and hydrazine hydrate (85%, 0.54 g, 9.12 mM) was added. The reaction mixture was then heated and refluxed for 2 h. Subsequently, 3 mL of diluted hydrochloric acid was added. After purification through column chromatography, the pure product Compound h was obtained as a colorless oil (1.5 g, 62.3%).

1-(2-(Dimethylamino) ethyl)-3-((6*Z*,9*Z*,28*Z*,31*Z*)-heptatriaconta-6,9,28,31-tetraen-19-yl) Thiourea (Ionizable Lipid Compound DMT7). Compound h (0.8 g, 1.52 mM), 2-isothiocyanato-N,N-dimethylethan-1-amine (0.2 g, 1.52 mM), and 5 mL of anhydrous *N*,*N*-dimethylformamide (DMF) were combined in the reaction flask. Following the reaction and purification via column chromatography, compound DMT7 was obtained in its pure form as a colorless oil (0.58 g, 58.2%). The synthetic route of DMT7 is described in Figure S3 and ionizable amino lipids DMT8, MPZT10, and MPZT11 can be synthesized using the same method described above.

(6*Z*,9*Z*,28*Z*,31*Z*)-19-Isothiocyanatoheptatriaconta-6,9,28,31-tetraene (Compound (i)). Compound h (1.5 g, 2.84 mM) and 10 mL of anhydrous THF were combined in the reaction flask, followed by the addition of *N*,*N*′-dicyclohexylcarbodiimide (DCC, 1.17 g, 5.68 mM). CS2 was then added dropwise in an ice bath. Following the reaction and purification via column chromatography, Compound i was obtained in its pure form as a colorless oil (1.1 g, 67.9%).

***N*-((6*Z*,9*Z*,28*Z*,31*Z*)-Heptatriaconta-6,9,28,31-tetraen-19-yl)-4-methylpiperazine-1carbothioamide (Ionizable Lipid Compound MPZT9).** Compound i (0.5 g, 0.88 mM) and 1-methylpiperazine (0.09 g, 0.88 mM) were dissolved in 3 mL of anhydrous DMF. Following the reaction and purification via column chromatography, compound MPZT9 was obtained in its pure form as a colorless oil (0.31 g, 52.7%). The synthetic route of MPZT9 is described in Figure S4.

Formulations of Lipid Nanoparticles and Encapsulation of mRNAs. To encapsulate mRNAs into diverse LNPs, a lipid mixture was formulated with mRNA in sodium acetate buffer solution (pH 4.6, 25 mM) using a microfluidic device (Micro&Nano, China). The weight ratio of lipid components in the mixture is 25:40:50:2, including cholesterol (Sigma-Aldrich, provided at 6 mg/mL in ethanol), DOPE (Avanti, at 3 mg/mL in ethanol), ionizable lipids (Avanti, supplied at 10 mg/mL in ethanol), and DMG-PEG2000 (Avanti, at 2.5 mg/mL in ethanol). Subsequently, the mixture was placed in a dialysis cassette with a 3500 molecular weight and dialyzed against PBS for 1 h at 25 °C to purify the nanoparticles and remove residual solvents. Concurrently, encapsulation of mRNAs into Lipofectamine Messenger MAX nanoparticles was carried out strictly in accordance with the manufacturer's instructions provided by Thermo Fisher Scientific.

Characterization of mRNA-Encapsulated LNPs. The morphological structure and hydrodynamic diameter of ALC-0315/DMT7-mRNA were accurately determined using TEM and DLS, respectively. For TEM analysis, 5 μL of DMT7-mRNA LNPs was meticulously placed onto a TEM copper grid. Following a 1 min settling period, excess liquid was gently removed by blotting with Kimwipes. Next, 5 μL of 1% uranyl acetate solution was added to stain the LNP samples for another minute. The stained samples were subsequently rinsed

https://doi.org/10.1021/acsnano.4c00063
ACS Nano 2024, 18, 15499−15516

with distilled water and left to air-dry in a fume hood. To evaluate the prolonged in vitro stability of ALC-0315/DMT7-mRNA, the LNPs were subjected to incubation in PBS and cell culture medium at 37 °C. The hydrodynamic diameters of the LNPs were assessed at different time intervals (0, 1, 3, 5, and 7 days) to monitor any changes over time.

Protection Assay. DMT7 LNP containing *GFP* mRNA or naked mRNA (200 ng) was exposed to FBS (5 μL) or varying concentrations of RNase A (ranging from 0 to 150 μg/mL) at RT for specified durations. Subsequently, the reactions were terminated by adding proteinase K (1 mg/mL). Following this, the samples were separated on a 1% agarose gel and subjected to visualization using an advanced imaging system (Biorad) for analysis.

Susceptibility of DMT7 LNP to Serum-Induced Aggregation. This assay was performed following a previously described protocol with slight modifications.[55] To assess the aggregation state of DMT7 LNPs, formulations containing *GFP* mRNA (100 ng) were subjected to incubation with 10% FBS at either RT or 37 °C. Subsequently, the absorbance at a wavelength of 660 nm was recorded using a microplate reader (Tecan, Switzerland) to monitor any changes in aggregation status.

Cellular Uptake and Lysosomal Escape of mRNA-Encapsulated LNPs. To assess the uptake of LNPs, Cy5-labeled mRNA-encapsulated ALC-0315 LNPs or Cy5-labeled mRNA-encapsulated DMT7 LNPs were prepared. Initially, B16F10 cells were plated into confocal dishes (Costar) at a density of 3×10^5 cells per dish and cultured at 37 °C for 15 h to facilitate cell attachment and growth. Subsequently, the cells were incubated with Cy5-mRNA-ALC-0315 LNPs or Cy5-mRNA-DMT7 LNPs in culture medium for 2, 4, or 8 h, respectively. Following the incubation, the cells were gently washed with PBS to remove any unbound LNPs. Finally, the cells were observed and analyzed using an Olympus microscope to visualize and quantify the intracellular localization and uptake of the Cy5-labeled LNPs.

Cell Viability Assay. B16F10 cells were seeded at a density of 1×10^4 cells per well in a 96-well plate and cultured overnight for cell attachment. Subsequently, the cells were treated with various concentrations of free mRNA, ALC-0315-mRNA LNPs, or DMT7-mRNA LNPs for a duration of 24 h. A group of cells that received no treatment served as the control. After the treatment period, the culture medium was substituted with fresh complete medium supplemented with the CCK8 reagent, and the plate was then incubated at 37 °C for 2 h. The absorbance at 490 nm was then recorded using a plate reader (Tecan, Switzerland).

Treatment of Contralateral B16F10 Tumors. To establish contralateral B16F10 tumors, female C57BL/6 mice weighing 20−22 g were implanted subcutaneously with 1×10^6 B16F10 cells in the right flank on day 0, followed by the injection of another 3×10^5 B16F10 cells into the left rear flank on day 2. Once the tumors reached a size range of 20−50 mm^3, approximately 7−9 days later, the animals were treated intratumorally with either PBS (control), 150 μg of free MSA-2, or 10 μg of *IL12* mRNA encapsulated in DMT7 LNPs, dissolved in approximately 100 μL of PBS, as indicated. The dosages of MSA-2 and *IL12* mRNA used for treatment were based on previously published studies.[8,56,57] In addition, some groups were subjected to combinatorial immunotherapy, receiving intraperitoneal injections of 100 μg of a checkpoint inhibitor (anti-PD-1 mAb). Tumor sizes were monitored every 2 days, and the average tumor volume was calculated using the formula: 1/2 × (length × width × width).

Treatment of Metastatic 4T1 Tumors. Female Balb/c mice (20−22 g) were injected with 1×10^6 4T1 cells into the fourth mammary fat pad. Seven to 9 days later, when tumors reached a size of 20−50 mm^3, animals were intratumorally injected with PBS (control), free MSA-2 (150 μg), or DMT7-IL12 (10 μg mRNA) in approximately 100 μL of PBS as indicated. For combinatorial immunotherapy, certain groups received intraperitoneal injections of 100 μg checkpoint inhibitor (anti-PD-1 mAb). Tumor sizes were assessed and calculated utilizing the aforementioned formula. Mice were euthanized on day 30. Lung tissues were preserved in 4% paraformaldehyde, and metastatic foci on the lungs were counted. After counting, the stained lung tissues underwent further staining with H&E. Metastatic tumor cell quantification in the H&E-stained sections was conducted using an Aperio Image Scope, aided by the tuned positive pixel count algorithm.

IVIS Spectrum Imaging Analysis. Female mice bearing 4T1 tumors received Cy7-labeled DMT7 LNPs via tail vein injection to assess their biodistribution. Fluorescence signals were captured using the In Vivo Imaging System (IVIS, PerkinElmer). Pharmacokinetic (PK) parameters were evaluated by quantifying the fluorescence intensity of Cy5-labeled DMT7 LNPs in the bloodstream at each designated time point. Subsequent to injection, tumor tissues and other organs, including the heart, liver, spleen, lung, and kidney, were excised for ex vivo fluorescence analysis utilizing the same imaging system.

Flow Cytometry Analysis. Flow cytometry was employed to analyze tumor-associated immune cell populations in tumor tissues, lungs, and serum. Antibodies against various mouse immune markers, including Ly6g (clone 1A8), CD45 (clone 30-F11), Ly6c (clone HK1.4), F4/80 (clone BM8), CD4 (clone GK1.5), CD3 (clone 17A2), CD11b (clone M1/70), CD25 (clone BC96), CD86 (clone GL-1), CD206 (clone C068C2), Foxp3 (clone 259D), NK1.1 (clone PK136), CD8a (clone 53−6.7), and IFN-γ (clone XMG1.2), were sourced from BioLegend. All antibodies were diluted to a 1:100 ratio for use in the analysis. Additionally, the live/dead dye Violet Zombie (catalog number 423107) was also obtained from BioLegend and diluted at a ratio of 1:500 for accurate cell viability assessment.

Flow cytometry analysis of $CD8^+$ T cells in tumor tissues: antibodies against mouse IFN-γ (clone XMG1.2), CD3 (clone 145−2C11), CD8a (clone 53−6.7), Granzyme B (clone QA18A28), TNF-α (clone MP6-XT22), CD366 (Tim-3) (clone RMT3−23), and CD279 (PD-1) (clone 29F.1A12) were from BioLegend. All of the antibodies from BioLegend were diluted at a ratio of 1:100. The live/dead dye Violet Zombie (catalog number 423107) was also obtained from BioLegend (diluted 1:500).

The tumor-bearing mice were humanely euthanized, and their tumors were excised and sliced into small fragments. These tumor fragments were then enzymatically digested using collagenase IV (1 mg/mL, Thermo Fisher Scientific) for a duration of 1 h at 37 °C to dissociate the cells into a single-cell suspension. Subsequently, the suspensions were passed through 70 μm nylon strainers to eliminate any residual debris and cell clumps. The filtered cells were then stained following the established protocol and were analyzed using a FACSCalibur flow cytometry system (BD Biosciences, California). All flow cytometry data were processed and analyzed utilizing FlowJo v10 software. The gating strategy utilized to identify each distinct immune cell population is presented in Figures S34−S40.

H&E Staining for Tissues. Tissues from tumors and various organs, including the heart, liver, spleen, lung, and kidney, were processed for histological examination. The tissues were fixed in paraformaldehyde, embedded in paraffin, and sectioned into thin slices with 10 μm thickness. Subsequently, the sections were deparaffinized and rehydrated to prepare them for further staining procedures. To enhance the antigenicity of the tissues, the sections were boiled in a 10 mM citrate buffer (pH 6.0) at 95 °C for 15 min. For H&E staining, an assay kit from Servicebio (China) was utilized, following the manufacturer's guidelines. The stained sections were then processed and analyzed using optical imaging techniques and the ImageJ Fiji software.

ELISA Assay. The tumor tissue was meticulously homogenized using a Precellys 24 Dual homogenizer in an ice-cold lysis buffer supplemented with protease and phosphatase inhibitors. Once homogenized, the lysates were centrifuged, and the supernatant was collected. Subsequently, the supernatant was assayed using ELISA kits from NeoBioscience to precisely quantify the levels of IL-12. Additionally, the concentrations of IL-2, TNF-α, and IFN-γ in the tumor tissues were accurately determined using the ELISA assay.

Statistical Analysis. Data collected from a minimum of three independent experiments were presented as mean ± SD. The statistical significance of differences between groups was determined

https://doi.org/10.1021/acsnano.4c00063
ACS Nano 2024, 18, 15499−15516

using either Student's *t*-test or one-way analysis of variance (ANOVA). A p-value less than 0.05 was considered statistically significant and was denoted as follows: $*p < 0.05$, $**p < 0.01$, $***p < 0.001$, and $****p < 0.001$.

ASSOCIATED CONTENT

Supporting Information

The Supporting Information is available free of charge at https://pubs.acs.org/doi/10.1021/acsnano.4c00063.

Representative synthetic route used to prepare ionizable amino lipid compounds (Figures S1−S4); characterization of 11 ionizable amino lipid by ^{1}H NMR spectra (Figures S5−S15); characterization of LNPs under different conditions (Figures S16 and S17); ELISA analysis of IL-12 p70 expression in B16F10 tumor tissues (Figure S18); stability of LNPs under different conditions (Figures S19 and S20); ELISA analysis of IL-12 p70 expression in B16F10 and 4T1 cell lines (Figure S21); stability of LNPs under different conditions (Figure S22); LNPs escape from endo/lysosomes (Figure S23); analysis of GFP expression by flow cytometry (Figures S24 and S25); ELISA analysis of IL-12 p70 expression in B16F10 cell lines (Figure S26); evaluation of antitumor activity of free MSA-2 in the B16F10 melanoma model (Figure S27); ELISA analysis of IFN-γ and IL-12 p70 levels in blood samples (Figure S28); biodistribution, pharmacokinetics, histochemistry analysis, and safety evaluation of DMT7 LNPs (Figures S29−S33); gating strategy used for flow cytometry analysis (Figures S34−S40); pK_a values of different ionizable amino lipids (Table S1); mRNA encapsulation efficiency of different LNPs (Table S2); size and sequence of mRNA (Table S3) (PDF)

AUTHOR INFORMATION

Corresponding Authors

Xiuling Li − *Shanghai Institute of Biological Products Co., Ltd., Shanghai 200051, China*; Email: lixiuling@sinopharm.com

Xiaoyang Xu − *Department of Chemical and Materials Engineering and Department of Biomedical Engineering, New Jersey Institute of Technology, Newark, New Jersey 07102, United States*; orcid.org/0000-0002-1634-3329; Email: xiaoyang.xu@njit.edu

Xue-Qing Zhang − *Shanghai Frontiers Science Center of Drug Target Identification and Delivery, School of Pharmaceutical Sciences, National Key Laboratory of Innovative Immunotherapy, Shanghai Jiao Tong University, Shanghai 200240, China*; orcid.org/0000-0002-4954-2586; Email: xueqingzhang@sjtu.edu.cn

Authors

Bin Wang − *Shanghai Frontiers Science Center of Drug Target Identification and Delivery, School of Pharmaceutical Sciences, National Key Laboratory of Innovative Immunotherapy, Shanghai Jiao Tong University, Shanghai 200240, China*

Maoping Tang − *Shanghai Frontiers Science Center of Drug Target Identification and Delivery, School of Pharmaceutical Sciences, National Key Laboratory of Innovative Immunotherapy, Shanghai Jiao Tong University, Shanghai 200240, China*

Qijing Chen − *Shanghai Frontiers Science Center of Drug Target Identification and Delivery, School of Pharmaceutical Sciences, National Key Laboratory of Innovative Immunotherapy, Shanghai Jiao Tong University, Shanghai 200240, China*

William Ho − *Department of Chemical and Materials Engineering and Department of Biomedical Engineering, New Jersey Institute of Technology, Newark, New Jersey 07102, United States*

Yilong Teng − *Shanghai Frontiers Science Center of Drug Target Identification and Delivery, School of Pharmaceutical Sciences, National Key Laboratory of Innovative Immunotherapy, Shanghai Jiao Tong University, Shanghai 200240, China*

Xiaojian Xiong − *Shanghai Frontiers Science Center of Drug Target Identification and Delivery, School of Pharmaceutical Sciences, National Key Laboratory of Innovative Immunotherapy, Shanghai Jiao Tong University, Shanghai 200240, China*

Zhitong Jia − *Shanghai Frontiers Science Center of Drug Target Identification and Delivery, School of Pharmaceutical Sciences, National Key Laboratory of Innovative Immunotherapy, Shanghai Jiao Tong University, Shanghai 200240, China*

Complete contact information is available at: https://pubs.acs.org/10.1021/acsnano.4c00063

Author Contributions

$^{\perp}$B.W. and M.T. authors contributed equally. X.-Q.Z., X.X., M.T., and B.W. conceived the study and designed experiments. X.-Q.Z. and X.X. supervised the research. B.W. and M.T. performed most of the experiments and analyzed the data. B.W. and M.T. synthesized the mRNAs. Q.C., Y.T., and X.X. synthesized different ionizable lipids and provided technical support for the LNP formulations. X.-Q.Z., X.X., M.T., and B.W. wrote the manuscript. B.W. and M.T. performed all of the statistical analyses. X.L. verified the precise execution of the data statistics and analysis methods, and reviewed and edited the manuscript. X.-Q.Z., X.X., M.T., and B.W. edited and revised the manuscript.

Notes

The authors declare no competing financial interest.

ACKNOWLEDGMENTS

This research was funded by the National Key Research and Development Program of China (2023YFC2606003), "Open Competition to Select the Best Candidates" Key Technology Program for Nucleic Acid Drugs of NCTIB (Grant No. NCTIB2022HS02002), the Natural Science Foundation of Shanghai (23ZR1427600), and the Program of Shanghai Frontiers Science Center of Drug Target Identification and Delivery (ZXWH2170101).

REFERENCES

(1) Shae, D.; Becker, K. W.; Christov, P.; Yun, D. S.; Lytton-Jean, A. K. R.; Sevimli, S.; Ascano, M.; Kelley, M.; Johnson, D. B.; Balko, J. M.; Wilson, J. T. Endosomolytic polymersomes increase the activity of cyclic dinucleotide STING agonists to enhance cancer immunotherapy. *Nat. Nanotechnol.* **2019**, *14* (3), 269−278.

(2) Pan, B.-S.; Perera, S. A.; Piesvaux, J. A.; Presland, J. P.; Schroeder, G. K.; Cumming, J. N.; Trotter, B. W.; Altman, M. D.; Buevich, A. V.; Cash, B.; et al. An orally available non-nucleotide

STING agonist with antitumor activity. *Science* **2020**, *369* (6506), No. eaba6098.
(3) Sivick, K. E.; Desbien, A. L.; Glickman, L. H.; Reiner, G. L.; Corrales, L.; Surh, N. H.; Hudson, T. E.; Vu, U. T.; Francica, B. J.; Banda, T.; et al. Magnitude of Therapeutic STING Activation Determines CD8(+) T Cell-Mediated Anti-tumor Immunity. *Cell Rep.* **2018**, *25* (11), 3074−3085 e3075.
(4) McLane, L. M.; Abdel-Hakeem, M. S.; Wherry, E. J. CD8 T Cell Exhaustion During Chronic Viral Infection and Cancer. *Annu. Rev. Immunol.* **2019**, *37*, 457−495.
(5) Chin, E. N.; Yu, C.; Vartabedian, V. F.; Jia, Y.; Kumar, M.; Gamo, A. M.; Vernier, W.; Ali, S. H.; Kissai, M.; Lazar, D. C.; et al. Antitumor activity of a systemic STING-activating non-nucleotide cGAMP mimetic. *Science* **2020**, *369* (6506), 993−999.
(6) Chen, X.; Meng, F.; Xu, Y.; Li, T.; Chen, X.; Wang, H. Chemically programmed STING-activating nano-liposomal vesicles improve anticancer immunity. *Nat. Commun.* **2023**, *14* (1), No. 4584.
(7) Hu, J.; Sánchez-Rivera, F. J.; Wang, Z.; Johnson, G. N.; Ho, Y.-j.; Ganesh, K.; Umeda, S.; Gan, S.; Mujal, A. M.; Delconte, R. B.; et al. STING inhibits the reactivation of dormant metastasis in lung adenocarcinoma. *Nature* **2023**, *616* (7958), 806−813.
(8) Pan, B. S.; Perera, S. A.; Piesvaux, J. A.; Presland, J. P.; Schroeder, G. K.; Cumming, J. N.; Trotter, B. W.; Altman, M. D.; Buevich, A. V.; Cash, B.; et al. An orally available non-nucleotide STING agonist with antitumor activity. *Science* **2020**, *369* (6506), eaba6098.
(9) Propper, D. J.; Balkwill, F. R. Harnessing cytokines and chemokines for cancer therapy. *Nat. Rev. Clin. Oncol.* **2022**, *19* (4), 237−253.
(10) Vignali, D. A. A.; Kuchroo, V. K. IL-12 family cytokines: immunological playmakers. *Nat. Immunol.* **2012**, *13* (8), 722−728.
(11) Tugues, S.; Burkhard, S. H.; Ohs, I.; Vrohlings, M.; Nussbaum, K.; Berg, J. V.; Kulig, P.; Becher, B. New insights into IL-12-mediated tumor suppression. *Cell Death Differ.* **2015**, *22* (2), 237−246.
(12) Morgan, M. A.; Lange, L.; Schambach, A. Targeted cytokine delivery: cell therapy to remodel the pre-metastatic niche. *Signal Transduction Targeted Ther.* **2021**, *6* (1), 282.
(13) van Herpen, C. M.; Huijbens, R.; Looman, M.; de Vries, J.; Marres, H.; Van De Ven, J.; Hermsen, R.; Adema, G. J.; De Mulder, P. H. Pharmacokinetics and immunological aspects of a phase Ib study with intratumoral administration of recombinant human interleukin-12 in patients with head and neck squamous cell carcinoma: A decrease of T-bet in peripheral blood mononuclear cells. *Clin. Cancer Res.* **2003**, *9* (8), 2950−2956.
(14) Chiocca, E. A.; Yu, J. S.; Lukas, R. V.; Solomon, I. H.; Ligon, K. L.; Nakashima, H.; Triggs, D. A.; Reardon, D. A.; Wen, P.; Stopa, B. M.; et al. Regulatable interleukin-12 gene therapy in patients with recurrent high-grade glioma: Results of a phase 1 trial. *Sci. Transl. Med.* **2019**, *11* (505), eaaw5680.
(15) Agarwal, Y.; Milling, L. E.; Chang, J. Y. H.; Santollani, L.; Sheen, A.; Lutz, E. A.; Tabet, A.; Stinson, J.; Ni, K.; Rodrigues, K. A.; et al. Intratumourally injected alum-tethered cytokines elicit potent and safer local and systemic anticancer immunity. *Nat. Biomed. Eng.* **2022**, *6* (2), 129−143.
(16) Xue, D.; Moon, B.; Liao, J.; Guo, J.; Zou, Z.; Han, Y.; Cao, S.; Wang, Y.; Fu, Y.-X.; Peng, H. A tumor-specific pro-IL-12 activates preexisting cytotoxic T cells to control established tumors. *Sci. Immunol.* **2022**, *7* (67), No. eabi6899.
(17) Huang, X.; Kong, N.; Zhang, X. C.; Cao, Y. H.; Langer, R.; Tao, W. The landscape of mRNA nanomedicine. *Nat. Med.* **2022**, *28*, 2273−2287.
(18) Rohner, E.; Yang, R.; Foo, K. S.; Goedel, A.; Chien, K. R. Unlocking the promise of mRNA therapeutics. *Nat. Biotechnol.* **2022**, *40* (11), 1586−1600.
(19) Etxeberria, I.; Bolanos, E.; Quetglas, J. I.; Gros, A.; Villanueva, A.; Palomero, J.; Sanchez-Paulete, A. R.; Piulats, J. M.; Matias-Guiu, X.; Olivera, I.; et al. Intratumor Adoptive Transfer of IL-12 mRNA Transiently Engineered Antitumor CD8(+) T Cells. *Cancer Cell* **2019**, *36* (6), 613−629 e617.
(20) Kim, J.; Eygeris, Y.; Gupta, M.; Sahay, G. Self-assembled mRNA vaccines. *Adv. Drug Delivery Rev.* **2021**, *170*, 83−112.
(21) Hou, X. C.; Zaks, T.; Langer, R.; Dong, Y. Z. Lipid nanoparticles for mRNA delivery. *Nat. Rev. Mater.* **2021**, *6* (12), 1078−1094.
(22) Chen, J.; Ye, Z.; Huang, C.; Qiu, M.; Song, D.; Li, Y.; Xu, Q. Lipid nanoparticle-mediated lymph node-targeting delivery of mRNA cancer vaccine elicits robust CD8(+) T cell response. *Proc. Natl. Acad. Sci. U.S.A.* **2022**, *119* (34), No. e2207841119.
(23) Li, W.; Zhang, X.; Zhang, C.; Yan, J.; Hou, X.; Du, S.; Zeng, C.; Zhao, W.; Deng, B.; McComb, D. W.; et al. Biomimetic nanoparticles deliver mRNAs encoding costimulatory receptors and enhance T cell mediated cancer immunotherapy. *Nat. Commun.* **2021**, *12* (1), No. 7264.
(24) Li, Y.; Su, Z.; Zhao, W.; Zhang, X.; Momin, N.; Zhang, C.; Wittrup, K. D.; Dong, Y.; Irvine, D. J.; Weiss, R. Multifunctional oncolytic nanoparticles deliver self-replicating IL-12 RNA to eliminate established tumors and prime systemic immunity. *Nat. Cancer* **2020**, *1* (9), 882−893.
(25) Li, H. J.; van der Leun, A. M.; Yofe, I.; Lubling, Y.; Gelbard-Solodkin, D.; van Akkooi, A. C. J.; van den Braber, M.; Rozeman, E. A.; Haanen, J. B. A. G.; Blank, C. U.; et al. Dysfunctional CD8 T Cells Form a Proliferative, Dynamically Regulated Compartment within Human Melanoma. *Cell* **2019**, *176* (4), 775−789.
(26) Zheng, L.; Qin, S.; Si, W.; Wang, A.; Xing, B.; Gao, R.; Ren, X.; Wang, L.; Wu, X.; Zhang, J.; et al. Pan-cancer single-cell landscape of tumor-infiltrating T cells. *Science* **2021**, *374* (6574), No. abe6474.
(27) Oliveira, G.; Stromhaug, K.; Klaeger, S.; Kula, T.; Frederick, D. T.; Le, P. M.; Forman, J.; Huang, T.; Li, S.; Zhang, W.; et al. Phenotype, specificity and avidity of antitumour CD8(+) T cells in melanoma. *Nature* **2021**, *596* (7870), 119−125.
(28) Melero, I.; Castanon, E.; Alvarez, M.; Champiat, S.; Marabelle, A. Intratumoural administration and tumour tissue targeting of cancer immunotherapies. *Nat. Rev. Clin. Oncol.* **2021**, *18* (9), 558−576.
(29) Balood, M.; Ahmadi, M.; Eichwald, T.; Ahmadi, A.; Majdoubi, A.; Roversi, K.; Roversi, K.; Lucido, C. T.; Restaino, A. C.; Huang, S.; et al. Nociceptor neurons affect cancer immunosurveillance. *Nature* **2022**, *611* (7935), 405−412.
(30) Raskov, H.; Orhan, A.; Christensen, J. P.; Gogenur, I. Cytotoxic CD8(+) T cells in cancer and cancer immunotherapy. *Br. J. Cancer* **2021**, *124* (2), 359−367.
(31) Matsushita, H.; Hosoi, A.; Ueha, S.; Abe, J.; Fujieda, N.; Tomura, M.; Maekawa, R.; Matsushima, K.; Ohara, O.; Kakimi, K. Cytotoxic T lymphocytes block tumor growth both by lytic activity and IFNgamma-dependent cell-cycle arrest. *Cancer Immunol. Res.* **2015**, *3* (1), 26−36.
(32) Thommen, D. S.; Schumacher, T. N. T Cell Dysfunction in Cancer. *Cancer Cell* **2018**, *33* (4), 547−562.
(33) Bitounis, D.; Jacquinet, E.; Rogers, M. A.; Amiji, M. M. Strategies to reduce the risks of mRNA drug and vaccine toxicity. *Nat. Rev. Drug Discovery* **2024**, *23*, 1−20.
(34) Connors, J.; Joyner, D.; Mege, N. J.; Cusimano, G. M.; Bell, M. R.; Marcy, J.; Taramangalam, B.; Kim, K. M.; Lin, P. J. C.; Tam, Y. K.; et al. Lipid nanoparticles (LNP) induce activation and maturation of antigen presenting cells in young and aged individuals. *Commun. Biol.* **2023**, *6* (1), 188.
(35) Lee, Y.; Jeong, M.; Park, J.; Jung, H.; Lee, H. Immunogenicity of lipid nanoparticles and its impact on the efficacy of mRNA vaccines and therapeutics. *Exp. Mol. Med.* **2023**, *55* (10), 2085−2096.
(36) Hashimoto, M.; Kamphorst, A. O.; Im, S. J.; Kissick, H. T.; Pillai, R. N.; Ramalingam, S. S.; Araki, K.; Ahmed, R. CD8 T Cell Exhaustion in Chronic Infection and Cancer: Opportunities for Interventions. *Annu. Rev. Med.* **2018**, *69*, 301−318.
(37) Minn, A. J.; Wherry, E. J. Combination Cancer Therapies with Immune Checkpoint Blockade: Convergence on Interferon Signaling. *Cell* **2016**, *165* (2), 272−275.
(38) Chen, J.; Qiu, M.; Ye, Z.; Nyalile, T.; Li, Y.; Glass, Z.; Zhao, X.; Yang, L.; Chen, J.; Xu, Q. In situ cancer vaccination using lipidoid nanoparticles. *Sci. Adv.* **2021**, *7* (19), eabf1244.

https://doi.org/10.1021/acsnano.4c00063
ACS Nano 2024, 18, 15499−15516

(39) Boudreau, C. E.; Najem, H.; Ott, M.; Horbinski, C.; Fang, D.; DeRay, C. M.; Levine, J. M.; Curran, M. A.; Heimberger, A. B. Intratumoral Delivery of STING Agonist Results in Clinical Responses in Canine Glioblastoma. *Clin. Cancer Res.* **2021**, *27* (20), 5528−5535.
(40) Vonderheide, R. H. The Immune Revolution: A Case for Priming, Not Checkpoint. *Cancer Cell* **2018**, *33* (4), 563−569.
(41) Mudassar, F.; Shen, H.; O'Neill, G.; Hau, E. Targeting tumor hypoxia and mitochondrial metabolism with anti-parasitic drugs to improve radiation response in high-grade gliomas. *J. Exp. Clin. Cancer Res.* **2020**, *39* (1), 208.
(42) Jayaprakash, P.; Ai, M.; Liu, A.; Budhani, P.; Bartkowiak, T.; Sheng, J.; Ager, C.; Nicholas, C.; Jaiswal, A. R.; Sun, Y.; et al. Targeted hypoxia reduction restores T cell infiltration and sensitizes prostate cancer to immunotherapy. *J. Clin. Invest.* **2018**, *128* (11), 5137−5149.
(43) Vardhana, S. A.; Hwee, M. A.; Berisa, M.; Wells, D. K.; Yost, K. E.; King, B.; Smith, M.; Herrera, P. S.; Chang, H. Y.; Satpathy, A. T.; et al. Impaired mitochondrial oxidative phosphorylation limits the self-renewal of T cells exposed to persistent antigen. *Nat. Immunol.* **2020**, *21* (9), 1022−1033.
(44) Hashimoto, M.; Araki, K.; Cardenas, M. A.; Li, P.; Jadhav, R. R.; Kissick, H. T.; Hudson, W. H.; McGuire, D. J.; Obeng, R. C.; Wieland, A.; et al. PD-1 combination therapy with IL-2 modifies CD8(+) T cell exhaustion program. *Nature* **2022**, *610* (7930), 173−181.
(45) Lin, L.; Rayman, P.; Pavicic, P. G., Jr.; Tannenbaum, C.; Hamilton, T.; Montero, A.; Ko, J.; Gastman, B.; Finke, J.; Ernstoff, M.; et al. Ex vivo conditioning with IL-12 protects tumor-infiltrating CD8(+) T cells from negative regulation by local IFN-gamma. *Cancer Immunol., Immunother.* **2019**, *68* (3), 395−405.
(46) Pulendran, B. Learning immunology from the yellow fever vaccine: innate immunity to systems vaccinology. *Nat. Rev. Immunol.* **2009**, *9* (10), 741−747.
(47) Pulendran, B.; P, S. A.; O'Hagan, D. T. Emerging concepts in the science of vaccine adjuvants. *Nat. Rev. Drug Discovery* **2021**, *20* (6), 454−475.
(48) Zhang, D.; Wang, G. X.; Yu, X. L.; Wei, T.; Farbiak, L.; Johnson, L. T.; Taylor, A. M.; Xu, J. Z.; Hong, Y.; Zhu, H.; Siegwart, D. J. Enhancing CRISPR/Cas gene editing through modulating cellular mechanical properties for cancer therapy. *Nat. Nanotechnol.* **2022**, *17* (7), 777−787.
(49) Lin, Y. X.; Wang, Y.; Ding, J.; Jiang, A.; Wang, J.; Yu, M.; Blake, S.; Liu, S.; Bieberich, C. J.; Farokhzad, O. C.; et al. Reactivation of the tumor suppressor PTEN by mRNA nanoparticles enhances antitumor immunity in preclinical models. *Sci. Transl. Med.* **2021**, *13* (599), eaba9772.
(50) Liu, M.; Hu, S.; Yan, N.; Popowski, K. D.; Cheng, K. Inhalable extracellular vesicle delivery of IL-12 mRNA to treat lung cancer and promote systemic immunity. *Nat. Nanotechnol.* **2024**, *19*, 565−575.
(51) Sistigu, A.; Yamazaki, T.; Vacchelli, E.; Chaba, K.; Enot, D. P.; Adam, J.; Vitale, I.; Goubar, A.; Baracco, E. E.; Remedios, C.; et al. Cancer cell-autonomous contribution of type I interferon signaling to the efficacy of chemotherapy. *Nat. Med.* **2014**, *20* (11), 1301−1309. Article.
(52) Wang, P.; Li, X.; Wang, J.; Gao, D.; Li, Y.; Li, H.; Chu, Y.; Zhang, Z.; Liu, H.; Jiang, G.; et al. Re-designing Interleukin-12 to enhance its safety and potential as an anti-tumor immunotherapeutic agent. *Nat. Commun.* **2017**, *8*, 1395.
(53) Hu, C.; Li, G.; Mu, Y.; Wu, W.; Cao, B.; Wang, Z.; Yu, H.; Guan, P.; Han, L.; Li, L.; Huang, X. Discovery of Anti-TNBC Agents Targeting PTP1B: Total Synthesis, Structure-Activity Relationship, In Vitro and In Vivo Investigations of Jamunones. *J. Med. Chem.* **2021**, *64* (9), 6008−6020. Article.
(54) Jayaraman, M.; Ansell, S. M.; Mui, B. L.; Tam, Y. K.; Chen, J.; Du, X.; Butler, D.; Eltepu, L.; Matsuda, S.; Hope, M. J.; et al. Maximizing the potency of siRNA lipid nanoparticles for hepatic gene silencing in vivo. *Angew. Chem., Int. Ed.* **2012**, *51* (34), 8529−8533. Article.
(55) Li, M.; Li, S.; Huang, Y.; Chen, H.; Zhang, S.; Zhang, Z.; Wu, W.; Zeng, X.; Zhou, B.; Li, B. Secreted Expression of mRNA-Encoded Truncated ACE2 Variants for SARS-CoV-2 via Lipid-Like Nanoassemblies. *Adv. Mater.* **2021**, *33* (34), No. e2101707.
(56) Li, Y.; Su, Z.; Zhao, W.; Zhang, X.; Momin, N.; Zhang, C.; Wittrup, K. D.; Dong, Y.; Irvine, D. J.; Weiss, R. Multifunctional oncolytic nanoparticles deliver self-replicating IL-12 RNA to eliminate established tumors and prime systemic immunity. *Nat. Cancer* **2020**, *1* (9), 882−893.
(57) Cirella, A.; Bolanos, E.; Di Trani, C. A.; de Andrea, C. E.; Sanchez-Gregorio, S.; Etxeberria, I.; Gonzalez-Gomariz, J.; Olivera, I.; Brocco, D.; Glez-Vaz, J.; Luri-Rey, C.; Azpilikueta, A.; Rodriguez, I.; Fernandez-Sendin, M.; Egea, J.; Eguren, I.; Sanmamed, M. F.; Palencia, B.; Teijeira, A.; Berraondo, P.; Melero, I. Intratumoral Gene Transfer of mRNAs Encoding IL12 in Combination with Decoy-Resistant IL18 Improves Local and Systemic Antitumor Immunity. *Cancer Immunol. Res.* **2023**, *11*, 184−198.

https://doi.org/10.1021/acsnano.4c00063
ACS Nano 2024, 18, 15499−15516